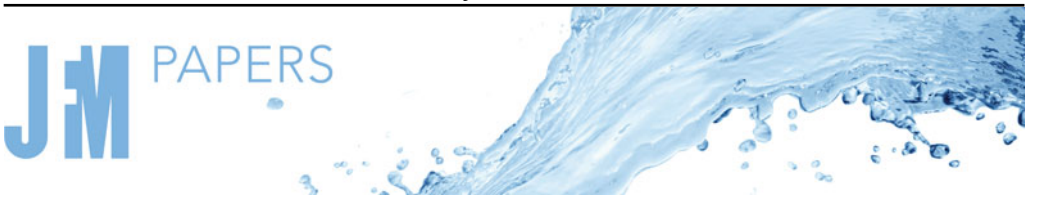
J. Fluid Mech. (2025), *vol.* 1018, A14, doi:10.1017/jfm.2025.10499



A leaky-dielectric fluid pump

Michael D. Mayer[1], **Toby L. Kirk**[2] **and Darren G. Crowdy**[1]

[1]Department of Mathematics, Imperial College London, 180 Queen's Gate, London SW7 2AZ, UK

[2]School of Mathematical Sciences, University of Southampton, Southampton SO17 1BJ, UK

Corresponding author: Toby L. Kirk, t.l.kirk@soton.ac.uk

(Received 20 December 2024; revised 17 June 2025; accepted 12 July 2025)

This paper theoretically introduces a new architecture for pumping leaky-dielectric fluids. For two such fluids layered in a channel, the mechanism utilises Maxwell stresses on fluid interfaces (referred to as menisci) induced by a periodic array of electrode pairs inserted between the two fluids and separated by the menisci. The electrode pairs are asymmetrically spaced and held at different potentials, generating an electric field with variation along the menisci. To induce surface charge accumulation, an electric field (and thus current flow) is also imposed in the direction normal to the menisci, using flat upper and lower electrodes, one in each fluid. The existence of both normal and tangential electric fields gives rise to Maxwell stresses on each meniscus, driving the flow in opposite directions on adjacent menisci. If the two menisci are the same length, then a vortex array is generated that results in no net flow; however, if the spacing is asymmetric, then the longer meniscus dominates, causing a net pumping in one direction. The pumping direction can be controlled by the (four) potentials of the electrodes, and the electrical properties of the two fluids. In the analysis, an asymptotic approximation is made that the interfacial electrode period is small compared to the fluid layer thicknesses, which reduces the analytical difficulty to an inner region close to the menisci. Closed-form solutions are presented for the potentials, velocity field and resulting pumping speed, for which maximum values are estimated, with reference to the electrical power required and feasibility.

Key words: dielectrics, electrokinetic flows, microfluidics

1. Introduction

Applications for microscale pumping mechanisms span areas from biology and medicine to microelectronics cooling. Although pumping mechanisms and design can vary widely, all micropumps are united in their objective to move small volumes of fluid (Laser &

© The Author(s), 2025. Published by Cambridge University Press. This is an Open Access article, distributed under the terms of the Creative Commons Attribution licence (https://creativecommons.org/licenses/by/4.0/), which permits unrestricted re-use, distribution and reproduction, provided the original article is properly cited.

https://doi.org/10.1017/jfm.2025.10499 Published online by Cambridge University Press

Santiago 2004). In this microfluidic regime, interfacial effects tend to dominate over volumetric ones, and the standard pressure-driven pumps available at the macroscale lose their efficacy (Stone, Stroock & Ajdari 2004). As a consequence, numerous pumping mechanisms have been considered that rely on interfacial phenomena. One in particular that has received significant attention is in the field of electrokinetics (Bazant & Squires 2010).

Electrokinetics is generally divided into electroosmosis (electrokinetically driven flow around stationary objects) and electrophoresis (electrokinetically driven motion of bulk particles) (Squires & Bazant 2004). Both rely on the formation of a charged double layer that forms when a conductive liquid such as an aqueous salt solution comes into contact with a charged surface. Then an electric field native to the system interacts with the charged layer, generating a force and driving flow. Although the driving mechanism is technically a body force acting on the double layer, the length scale of this charged layer is quite small, leading to large velocity gradients in the fluid and flows that often take the appearance of a plug flow. As a consequence, electroosmotic effects are commonly modelled as a given tangential velocity at the solid interface, known as the Helmholtz–Smoluchowski slip velocity (Squires & Bazant 2006).

Generally, research on electroosmotic pumping has been on solid–liquid interfaces; however, it has also been considered for liquid–liquid interfaces (Pascall & Squires 2011). In Pascall & Squires (2011), a conductive liquid was considered to rest atop a thin liquid film consisting of either a liquid metal or finite conductivity liquid. In the former case the electrical physics is very similar to when the surface is solid; however, the hydrodynamic coupling of the two liquids led to a flow enhancement over the solid wall case. Interestingly, the leading order of the analysis of Pascall & Squires (2011) matched that of earlier work by Frumkin (1946) (also presented in Levich 1962) in investigations of the electrophoresis of liquid metal drops. Instead of directly considering the double layer, Frumkin and Levich argued that spatially varying zeta potentials led to gradients in surface tension via the Lippman equation,

$$\gamma(V) = \gamma_{eq} - \frac{qV}{2}, \tag{1.1}$$

causing electrocapillary motion. Here, γ is the surface tension, γ_{eq} is the surface tension in the absence of electric fields, q is the excess charge per area of the interface, and V is the voltage drop across the double layer. This showed that the thermodynamic origins of the Lippman equation were insufficient to capture the subdominant effects caused by the double layer. In the case when both liquids have finite conductivities, both fluids develop charged double layers. However, Pascall & Squires (2011) showed that the electric stress from the Lorentz force in the thin film was perfectly balanced by the osmotic pressure due to gradients in charge concentration. Therefore, as when the internal fluid was a liquid metal, only hydrodynamic stresses were left to balance the electrokinetic stress in the outer fluid, leading to predicted slip velocities that differed only slightly from the case when the internal liquid was a metal.

Another pillar of electrohydrodynamics is the study of leaky-dielectric fluids. Melcher & Taylor (1969) developed the canonical model of these fluids after Taylor (1966) noticed a significant physical difference in systems where the fluids were pure dielectrics (perfectly non-conducting) and ones that have a finite, but small conductivity. In the case of the latter, interfacial charge build-up can have significant impacts on flows, most importantly causing Maxwell stresses on fluid–fluid interfaces. Traditionally, the fields of electrokinetics (specifically concerning electrolytes) and leaky dielectrics have been pursued independently (Saville 1997); however, some attempts have been made to connect

https://doi.org/10.1017/jfm.2025.10499 Published online by Cambridge University Press

the two. Zholkovskij, Masliyah & Czarnecki (2002) considered general electrokinetic equations, and took the limit of small electric field and small double-layer thickness, showing agreement for calculations on drop deformation with Taylor (1966). Schnitzer & Yariv (2015) showed that in taking the double limit of large electrical field and small double-layer thickness, classical electrokinetic theory reduces to the Taylor–Melcher leaky-dielectric model without surface charge advection. This corresponds to the low electric Reynolds number limit, which was consistent with their asymptotic analysis. Schnitzer & Yariv (2015) built on prior work by Baygents & Saville (1990), and this was a large step in unifying the two fields of research (Bazant 2015). Mori & Young (2018) were able to derive the full Taylor–Melcher model from general electrokinetic equations by assuming that the fluids were weak electrolytes along with the typical assumption of small double-layer thickness. More recently, the work by Mori & Young (2018) was corroborated by López-Herrera *et al.* (2023) in a numerical simulation of electrospray. Their work also investigated where the leaky-dielectric model became invalid, which, not surprisingly, was for strong electrolytes where charge inhomogeneities developed.

Although electrokinetics and the Taylor–Melcher leaky-dielectric model are clearly related, most research into pumping remains in the electrokinetic regime, with leaky-dielectric research seemingly mostly related to liquid drops (Sherwood 1988; Feng 1999, 2002; Salipante & Vlahovska 2010; He, Salipante & Vlahovska 2013; Schnitzer, Frankel & Yariv 2013; Lanauze, Walker & Khair 2015; Das & Saintillan 2017). However, pumping oils has significant implications in applications. This includes microfluidics, where converging flows of oil are often used to pinch and generate water droplets to use in e.g. mixing of reagents for high throughput assays, and synthesis of microparticles or nanoparticles (Belousov *et al.* 2021) (see Moragues *et al.* (2023) for more on the use of oil in droplet-based microfluidics). Therefore, finding novel means of pumping oils appear to be valuable. Two challenging aspects of a leaky-dielectric pump are as follows. The first is that the driving mechanism, Maxwell stress, acts on liquid interfaces, i.e. solid–liquid and liquid–liquid. Examples of solid–liquid include dielectrophoresis and the Quincke rotation of solid particles suspended within a liquid. However, an experimental set-up to realise a tangential electric field in a channel, and thereby channel flow generation, is less clear. A pump utilising Maxwell stresses at liquid–liquid interfaces is another option, but the design configuration may be complicated. A second challenge is that Maxwell stresses, given for a flat mensicus or liquid–liquid interface by

$$\sigma_M \propto E_t E_n, \tag{1.2}$$

require the electric field at the interface to have both a tangential (E_t) and normal (E_n) component. This second point precludes even a simple pump consisting of two leaky dielectrics in a channel due to the large voltage drop needed to generate a significant electric field in the direction of the flow.

Perhaps a more feasible pumping design would be motivated by Ajdari (2000), who demonstrated an electrokinetic pump that only required local gradients (i.e. microscale not macroscale gradients) in potential along the surface. His pump surface consisted of a series of finite length electrodes separated by electrically insulating material. He showed that geometric asymmetry, in his case modifications to the capacitance of the surface, led to a net pumping even when the electric field was periodic in time and space. The crux of his work was that 'any fluid in a *locally* asymmetric geometry *globally* drifts in the direction of broken symmetry under any external action that induces *local* flows' (Ajdari 2000). This concept was confirmed experimentally by Brown, Smith & Rennie (2001), who fabricated a pump with alternating long and short electrodes, demonstrating pumping. The role of geometric asymmetry in electrokinetics was further investigated by

https://doi.org/10.1017/jfm.2025.10499 Published online by Cambridge University Press

Squires & Bazant (2006) for a variety of problems related to both electroosmosis (in the context of microfluidic flows) and electrophoresis (in the context of colloids). Moreover, this phenomenon has appeared accidentally, as in work by Mansuripur, Pascall & Squires (2009), who set out to investigate symmetric vortices induced by electroosmotic flow, but observed a net pumping caused by symmetry breaking due to capacitive coupling between the electrode gate and the microscope stage. Outside of electrokinetics, Crowdy, Mayer & Hodes (2023) showed that thermocapillary stress can cause far-field pumping for liquids suspended over superhydrophobic surfaces. There, the asymmetry is provided by differing lengths of periodic pairs of menisci between alternating hot and cold substrate microstructures. This design has the advantage of using local periodic temperature gradients to pump flow without the need for an average global temperature gradient.

Pulling from the symmetry-breaking ideas of Ajdari (2000), we theoretically demonstrate the viability of a new microfluidic pump architecture for leaky-dielectric fluids. The pump consists of two leaky-dielectric fluids with a periodic array of pairs of thin electrodes, unequally spaced, inserted at the fluid–fluid interface. Between the electrodes, the fluids are in contact. Crucially, the fluids are pinned to the electrode edges due to their own surface tension, which requires fluids that are immiscible: e.g. castor oil and silicone oil form one such pair, but other immiscible leaky dielectrics are common. The surface tension adds mechanical stability to this set-up similar to what happens in a superhydrophobic surface, or even more relevant, a slippery liquid-infused porous surface (SLIPS). Wang & Guo (2020) provide a review and comparison of superhydrophobic surfaces and SLIPS. Such liquid–liquid configurations, pinned by surface tension across microscale pores/openings, have been shown to be remarkably robust, even supporting the dynamic rolling of droplets.

A schematic of the proposed pump is in figure 1. The two electrodes that make up a pair are held at different potentials so that on moving along the channel, the electrode potentials alternate. This means that there is no net electric field along the channel, but local tangential components to the electric field are induced. A necessary normal component to the electric field is forced by flowing a current through the fluids from a flat upper electrode to a flat lower electrode. The resulting Maxwell stresses drive flow along the fluid–fluid interfaces (hereafter referred to as menisci) in opposite directions. Crucially, since the menisci lengths differ, one dominates the other, leading to net fluid pumping in one direction. This direction of flow is shown to be a function of the electrode potentials and the electrical properties of the two fluids. In our analysis, surface charge advection is neglected, and the period is assumed to be small compared to the thicknesses of the two fluids (equivalently, the distance between the upper/lower electrodes) so that the method of matched asymptotic expansions can be used. The fluid domains then decompose into an ‘inner region’ close to the menisci, and ‘outer regions’ above and below where the fields appear one-dimensional (up to exponentially small errors). The general electrical problem in the inner region turns out to be a non-trivial two-phase problem, which is solved using a superposition of two different current flows: one is taken from an analogy with a thermocapillary pump (Crowdy *et al.* 2023), and the other is entirely new, and is described here in detail. As a result, we obtain explicit solutions for the potential fields and pumping speed, and analyse the optimal pumping configurations and give estimates for the maximum speeds achievable. Two geometric assumptions are made in our analysis: that the problem is two-dimensional (2-D), and that the menisci are flat. The 2-D assumption is often valid for channels that are wider than they are tall, which limits somewhat the practical applicability of this problem; however, the relevant physics remains the same. The menisci are assumed flat, which helps to facilitate analytical techniques, but it is shown later that the capillary number, defined as the ratio of viscous stresses to surface tension

https://doi.org/10.1017/jfm.2025.10499 Published online by Cambridge University Press

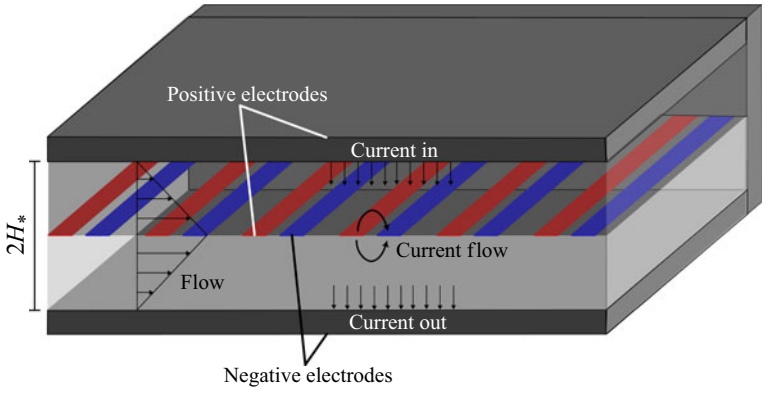


Figure 1. Schematic of the proposed pump architecture. Upper and lower electrodes encase two different fluids separated by an asymmetric array of electrodes with interfacial menisci spanning the gaps between them.

forces, is small for most physical scenarios, meaning that the menisci should be close to flat in practice.

The paper is organised as follows. The mathematical problem is formulated in § 2, and the small-period approximation (decomposing the problem into inner and outer regions) is detailed in § 3. The solutions for the potential in the inner region are presented, in two parts, in §§ 4 and 5, followed by those for the flow velocity in § 6, with expressions for power given in § 7. The results and discussion are given in § 8, with a (dimensional) summary of the theoretical formulas given in § 9. Finally, a discussion section closes the paper.

2. Problem formulation

We consider a 2-D microchannel of height $2H_*$ whose top and bottom walls are electrodes held at different constant voltages $V_{\perp *}^{+}$ and $-V_{\perp *}^{-}$, respectively. At $y_* = 0$, the midline of the channel, there exists an array of thin electrodes that are asymmetrically spaced but all assumed to be of equal width. Specifically, these electrodes appear in pairs in which the distance between the electrodes is unequal, leading to a periodic array of electrode pairs with structural asymmetry. Above and below this electrode array are two different leaky-dielectric fluids. To denote differences between the fluids, the parameters and variables related to the upper fluid are decorated with the superscript $+$, and the lower fluid with superscript $-$. For example, each liquid has its own dielectric conductivity $\sigma^{\pm}$, electric permittivity $\epsilon^{\pm}$, and viscosity $\mu^{\pm}$. A schematic of the domain and a summary of the problem is given in figure 2.

To examine this problem, we focus on a single period within this channel, containing two electrodes. The period is such that the right-hand side of the high potential electrode is located at $x_* = 0$. The period is denoted by D_*, the width of both electrodes is denoted by L_*, and the width of the meniscus to the right of the high potential electrode is S_*. Dimensional lengths and variables are indicated with an asterisk subscript.

According to the Melcher–Taylor leaky-dielectric model (Melcher & Taylor 1969), all charges accumulate on the fluid interfaces, so that the electric potentials $\phi_*^{\pm}$ are electroneutral and therefore, by Gauss' law, are harmonic in their respective domains:

$$\nabla_*^2 \phi_*^{\pm} = 0. \tag{2.1}$$

https://doi.org/10.1017/jfm.2025.10499 Published online by Cambridge University Press

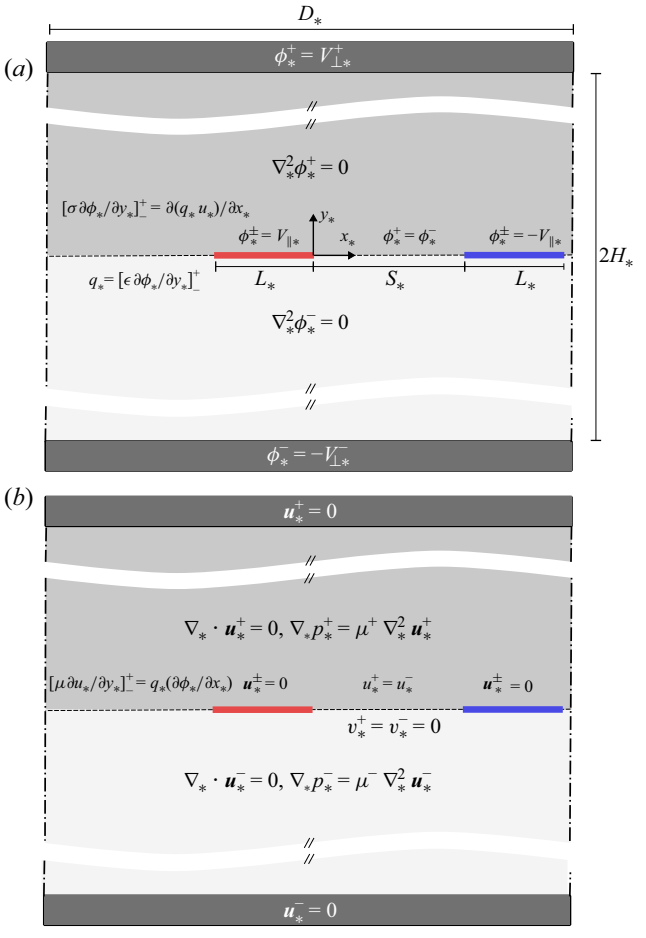


Figure 2. Problem domains for (*a*) the potential fields and (*b*) the velocity fields. Here, a periodic array of high and low potential electrodes separates two leaky-dielectric fluids. The electric field created by the electrodes, along with one generated by current flowing vertically through the system, generates Maxwell stresses on the menisci between electrodes, driving flow.

At $y_* = 0$, there is a mixed boundary condition where one of the electrodes is held at $\phi_*^\pm = V_{\parallel *}$, the other at $\phi_*^\pm = -V_{\parallel *}$, and at the menisci between the electrodes, the electrical potentials (and therefore tangential gradients) are continuous, but the normal component of the electric field undergoes a jump due to mismatches in the electric properties of the two fluids (Das & Saintillan 2017):

$$[\phi_*]_-^+ = 0 \quad \text{on the menisci,} \tag{2.2}$$

$$\left[\sigma \frac{\partial \phi_*}{\partial y_*}\right]_-^+ = \frac{\partial}{\partial x_*}(q_* u_*) \quad \text{on the menisci,} \tag{2.3}$$

where

$$q_* = -\left[\epsilon \frac{\partial \phi_*}{\partial y_*}\right]_-^+ \tag{2.4}$$

is the surface charge distribution. Again, $\sigma^\pm$, $\epsilon^\pm$, $\mu^\pm$ are the electrical conductivity, permittivity and viscosity, respectively. Additionally, there is a potential difference

https://doi.org/10.1017/jfm.2025.10499 Published online by Cambridge University Press

between the top and bottom electrodes,

$$\phi_*^+ = V_{\perp *}^+ \quad \text{at } y_* = H_*, \qquad \phi_*^- = -V_{\perp *}^- \quad \text{at } y_* = -H_*, \tag{2.5}$$

which ensures there is a normal electric field component at the menisci, needed for surface charge accumulation and therefore Maxwell stresses.

The velocity fields $\boldsymbol{u}_*^\pm = (u_*^\pm, v_*^\pm)$ are assumed to satisfy the Stokes equations, i.e.

$$\boldsymbol{\nabla}_* p_*^\pm = \mu^\pm \nabla_*^2 \boldsymbol{u}_*^\pm, \quad \boldsymbol{\nabla}_* \cdot \boldsymbol{u}_*^\pm = 0, \tag{2.6}$$

where $p_*^\pm$ denote pressures in the fluids. At the mixed boundary at $y^* = 0$, the electrodes are considered no-slip surfaces, while on the fluid interfaces, a tangential stress balance between shear stress and Maxwell stress leads to a coupling of the velocity and potential fields:

$$\boldsymbol{u}_*^\pm = \boldsymbol{0} \quad \text{on the electrodes,} \tag{2.7}$$

$$v_*^\pm = 0, \quad \left[\mu \frac{\partial u_*}{\partial y_*}\right]_-^+ = q_* \frac{\partial \phi_*^+}{\partial x_*} \quad \text{on the menisci.} \tag{2.8}$$

The no-slip condition is imposed on the top and bottom electrodes:

$$\boldsymbol{u}_*^\pm = \boldsymbol{0} \quad \text{at } y_* = \pm H_*. \tag{2.9}$$

Finally, both the potential and velocity fields are taken to be periodic with period D_*, closing the problem.

We have assumed here that the menisci are flat, which is equivalent to assuming that the effects of surface tension are large, i.e. that the capillary number Ca (ratio of viscous stresses to surface tension forces) is small. Given the small scale of the pump, and typical dielectric liquids that could be used, a small capillary number is a reasonable assumption in this case – see the next section. This means that the viscous terms in the normal stress balance at the meniscus could be neglected, giving a leading-order balance between curvature and pressure terms, i.e. $p_*^+ - p_*^- +$ negligible normal viscous stresses $= \gamma \kappa_*$, where κ_* is the curvature. However, the flow that we consider is driven not by a pressure gradient but by Maxwell stresses that appear in tangential stress, hence the pressure variations are purely periodic, driven by viscous effects, and thus scale with viscous stresses, $p_*^\pm \sim \mu^\pm U_{c*}/H^*$ (see the next subsection, where the problem is non-dimensionalised). Therefore, pressure variations are also negligible compared to the curvature for small capillary number, and the leading-order balance is in fact $\gamma \kappa_* \approx 0$. The lack of a macroscale pressure gradient then ensures that the menisci remain flat down the entire length of the pump. This flat assumption can be relaxed using additional analytical techniques, but that is outside the scope of this paper.

2.1. *Dimensionless formulation*

The potentials $\phi_*^\pm$ are made dimensionless using the potential scale $\phi_{c*} = V_{\parallel *}$ from the positive electrode on the interface, and q_* is made dimensionless using $\epsilon^+ \phi_{c*}/H_*$. Additionally, H_* is used as a length scale, $U_{c*} = \epsilon^+ \phi_{c*}^2/[H_*(\mu^+ + \mu^-)]$ is used as a velocity scale, and pressures $p_*^\pm$ are scaled with $\mu^\pm U_{c*}/H_*$. Then the capillary number can be defined as $Ca = (\mu^+ + \mu^-)U_{c*}/\gamma$, which, using liquid properties for silicone and castor oils (Salipante & Vlahovska 2010), and the example operating parameters given later in § 9, takes values of $O(10^{-3})$, small compared to 1. The dimensionless width of the electrodes becomes $\delta L = L_*/H_*$, where $\delta = D_*/H_*$ is the dimensionless period, and $L = L_*/D_*$ is the fraction of a period occupied by one electrode. Similarly, the

https://doi.org/10.1017/jfm.2025.10499 Published online by Cambridge University Press

dimensionless length of one meniscus (right of the positive electrode) is $\delta S = S_*/H_*$, where $S = S_*/D_*$ is the meniscus fraction. The equations for $\phi^{\pm}$ remain unchanged, but on the mixed boundary, the potential fields satisfy

$$\phi^{\pm} = 1 \qquad \text{on } y = 0, \text{ on the positive electrode } (-\delta L < x < 0), \tag{2.10}$$

$$\phi^{\pm} = -1 \qquad \text{on } y = 0, \text{ on the negative electrode } (\delta S < x < \delta S + \delta L), \tag{2.11}$$

$$\phi^{+} = \phi^{-} \qquad \text{on } y = 0, \text{ on the menisci}, \tag{2.12}$$

$$R\frac{\partial \phi^{+}}{\partial y} - \frac{\partial \phi^{-}}{\partial y} = Re_e \frac{\partial}{\partial x}(qu) \qquad \text{on } y = 0, \text{ on the menisci}, \tag{2.13}$$

where $Re_e = \epsilon^{+} U_{c*}/(\sigma^{-} H_*)$ is the electric Reynolds number, and $R = \sigma^{+}/\sigma^{-}$ is the ratio of the fluid conductivities. In the subsequent analysis, we set $Re_e = 0$, an assumption that is discussed later. The dimensionless charge is given by

$$q = -\left(\left.\frac{\partial \phi^{+}}{\partial y}\right|_{y=0} - Q \left.\frac{\partial \phi^{-}}{\partial y}\right|_{y=0} \right), \tag{2.14}$$

where $Q = \epsilon^{-}/\epsilon^{+}$ is a ratio of electric permittivities. The potential conditions on the top and bottom electrodes become

$$\phi^{\pm} = \pm V_{\perp}^{\pm} \quad \text{at } y = \pm 1. \tag{2.15}$$

The velocity field now satisfies the dimensionless Stokes equations

$$\nabla p^{\pm} = \nabla^2 \boldsymbol{u}^{\pm}, \quad \nabla \cdot \boldsymbol{u}^{\pm} = 0, \tag{2.16}$$

and at $y = 0$,

$$\boldsymbol{u}^{\pm} = \boldsymbol{0} \qquad \text{on the electrodes}, \tag{2.17}$$

$$u^{+} = u^{-} \qquad \text{on the menisci}, \tag{2.18}$$

$$v^{\pm} = 0 \qquad \text{on the menisci}, \tag{2.19}$$

$$m^{+}\frac{\partial u^{+}}{\partial y} - m^{-}\frac{\partial u^{-}}{\partial y} = q\frac{\partial \phi^{+}}{\partial x} \qquad \text{on the menisci}, \tag{2.20}$$

where $m^{\pm} = \mu^{\pm}/(\mu^{+} + \mu^{-})$. At the top and bottom electrodes, the no-slip conditions are

$$\boldsymbol{u}^{\pm} = 0 \quad \text{at } y = \pm 1. \tag{2.21}$$

Combined with the appropriate periodicity conditions, with period δ, the problem is now fully stated.

2.2. *Symmetry of the velocity fields*

It is useful at this stage to point out a surprising symmetry in the flow fields of the two fluids. The flows in both fluids are driven entirely by the tangential stress condition (2.20), in which the Maxwell stress forcing divides its action between the two fluids, and the division is in general different owing to their differing (non-dimensional) viscosities, i.e. $m^{\pm}$. But it turns out that if the flow domain is exactly symmetric about the interfacial plane $y = 0$ (which is assumed here), then the velocity fields in both fluids are identical up to reflection. To show this, imagine that $\boldsymbol{u}^{-}$ is known, and then the flow $\boldsymbol{u}^{+}$ satisfies the

https://doi.org/10.1017/jfm.2025.10499 Published online by Cambridge University Press

Stokes equations in $0 < y < 1$ with prescribed tangential velocities at $y = 0$ (where either $u^+ = 0$ or $u^+ = u^-$) and $y = 1$ (where $u^+ = 0$). Combined with the periodic boundary conditions in x, where p^+ is periodic with no linear component, this gives a unique solution for $\boldsymbol{u}^+$. The same argument applies in the lower fluid, $\boldsymbol{u}^-$, given a known menisci velocity u^+. The key observation is that u^+ and u^- on the menisci are the same by velocity continuity, even if they are not yet known, thus $u^\pm$ satisfy the same boundary value problems, up to reflection in $y = 0$, so

$$\boldsymbol{u}^-(x, y) = \boldsymbol{u}^+(x, -y). \tag{2.22}$$

Then on the menisci we have $\partial u^-/\partial y = -\partial u^+/\partial y$, which when substituted into (2.20) gives

$$\frac{\partial u^+}{\partial y} = q\frac{\partial \phi^+}{\partial x} \quad \text{on the menisci,} \tag{2.23}$$

using $m^+ + m^- = 1$. This means that even though the shear stresses experienced by each fluid on the menisci are different (owing to the differing viscosities), they are in exactly the right proportion so that the resulting velocity shear (and hence velocities) are the same magnitude and given by (2.23). This is true for any choice of liquid property (e.g. viscosity ratio, electric Reynolds number) and interfacial electrode configuration, the only requirement being geometrical symmetry about $y = 0$. Clearly, this will no longer hold if the two fluid layers are of different thicknesses.

It is important to remark that no similar symmetry exists in the electrical problems for $\phi^\pm$, hence both phases always must be considered for that problem. Hence it is convenient still to use the notation $u^\pm$ in the following sections for convenience, with the symmetry understood.

2.3. *Zero electric Reynolds number*

In the above problem description, (2.13) is a general form of current continuity for a flat meniscus. It states that any jump in current between the two fluids must be due to the advection of charge along the interface, and the degree to which charge advection occurs is determined by the value of the electric Reynolds number.

To obtain physical values of the relevant properties, we turn to Salipante & Vlahovska (2010), who examined the rotation of liquid drops of silicone oil ($\epsilon/\epsilon_0 = 3.0$, $\sigma = 1.23 \times 10^{-12}$ S m^{-1}, $\mu = 0.97$ kg m^{-1}s^{-1}) in castor oil ($\epsilon/\epsilon_0 = 5.3$, $\sigma = 4.5 \times 10^{11}$ S m^{-1}, $\mu = 0.69$ kg m^{-1}s^{-1}), where $\epsilon_0 \approx 8.85 \times 10^{-12}$ F m^{-1} is the permittivity of free space. With these values, the remaining factor in Re_e is ϕ_{c*}^2/H_*^2. Recalling that $\phi_{c*} = V_{\parallel *}$, we can then define a new parameter

$$E_{0*} = V_{\parallel *}/H_*, \tag{2.24}$$

where E_{0*} (units V m^{-1}) is a scale for the background electric field in the lower fluid. In this way, the electric Reynolds number can be rewritten as

$$Re_e = \frac{(\epsilon^+ E_{0*})^2}{\sigma^-(\mu^+ + \mu^-)}, \tag{2.25}$$

a form similar to that found in Das & Saintillan (2017).

An alternative definition that is perhaps more representative of the problem considered here is one with different scalings for the electric field in the x and y directions, which can be varied independently in our problem (and could differ by orders of magnitude). That is,

https://doi.org/10.1017/jfm.2025.10499 Published online by Cambridge University Press

Non-dimensional parameter	R	Q	m^+	$Re_{e,m}$	Ca
Value	0.027	1.7	0.59	3.4	0.006

Table 1. Representative values for non-dimensional parameter groups, using values for silicone oil (+ fluid) and caster oil (− fluid) (Salipante & Vlahovska 2010). Recall that $m^- = 1 - m^+$. Here, $V_{\parallel *} = 0.1$ kV, $V_{\perp *} = 2$ kV, $H_* = 1$ cm, and $D_* = 2$ mm, so that $E_{\parallel c*} = 5 \times 10^4$ V m^{-1}and $E_{\perp c*} = 2 \times 10^5$ V m^{-1}.

we can define characteristic electric field strengths

$$E_{\parallel c*} = V_{\parallel *}/D_*, \quad E_{\perp c*} = V_{\perp *}/H_*, \tag{2.26}$$

and also

$$Re_{e,m} = \frac{\epsilon^{+2} E_{\parallel c*} E_{\perp c*}}{\sigma^-(\mu^+ + \mu^-)} = \frac{\epsilon^{+2} V_{\parallel *} V_{\perp *}}{H_* D_* \sigma^-(\mu^+ + \mu^-)}, \tag{2.27}$$

which we call the modified electric Reynolds number. It captures variation in field strength both perpendicular and tangential to the interface. It is easy to see that $Re_{e,m} = Re_e\,(H_*/D_*)(V_{\perp *}/V_{\parallel *})$.

From (2.27), it is clear that the maximum value of $Re_{e,m}$ will occur in the pump when silicone oil is on the top, so we restrict ourselves to this case. Since the fluids are leaky dielectrics, electric field strengths can be quite large, with experimental maxima 4.5 kV cm^{-1} (Vizika & Saville 1992) in a study of small deformations of droplets, and 20 kV cm^{-1} (Salipante & Vlahovska 2010) in a study of spontaneous rotation of liquid drops under large electric fields. Taylor (1966) himself used two experimental values, $E_{0*} = 0.65$ kV cm^{-1} and $E_{0*} = 1.6$ kV cm^{-1}. However, to validate their experimental set-up, Salipante & Vlahovska (2010) tested and measured deformation of the drop in weak electric fields to enable comparison to Taylor's theory. They found that significant deviation began at electric field values approximately 1 kV cm^{-1}, which, assuming similar field strengths in the x and y directions, corresponds to $Re_{e,m} = 3.4$. This result is critical because it shows that deviations from the solutions by Taylor (1966) occurred when the electric Reynolds number became order 1, highlighting the importance of charge advection at large field strengths. Consequently, we posit that the small or zero electric Reynolds assumption is valid when $\sqrt{E_{\parallel c*} E_{\perp c*}} < 10^5$ V m^{-1}. Representative values of $Re_{e,m}$ at this maximal constraint, along with the other relevant dimensionless groups, can be found in table 1 using $E_{\parallel c*} = 5 \times 10^4$ V m^{-1} and $E_{\perp c*} = 2 \times 10^5$ V m^{-1}.

3. Bounded two-phase problem: small period limit

In this section, we analyse the problem detailed in § 2, where the two fluid layers are in a channel of finite thickness, i.e. are bounded by upper and lower electrodes at $y = \pm 1$, where the potential is specified, $\phi^{\pm} = \pm V_{\perp}^{\pm}$. A simplifying assumption is that the interfacial electrode period is small compared to the channel height, i.e. $\delta = D^*/H^* \ll 1$. The problem will then be reduced to finding a solution to a (still highly non-trivial) 'unbounded' problem, which appears as the local (or 'inner') solution close to the interface $y = 0$. The analysis of this section shows how that problem arises naturally within the channel problem, and what the far-field conditions should be, which is more practically relevant. The unbounded inner problem is then solved, in two parts, in §§ 4 and 5. Figure 3 gives a schematic showing how the domain is divided, and the structure of the inner problem.

https://doi.org/10.1017/jfm.2025.10499 Published online by Cambridge University Press

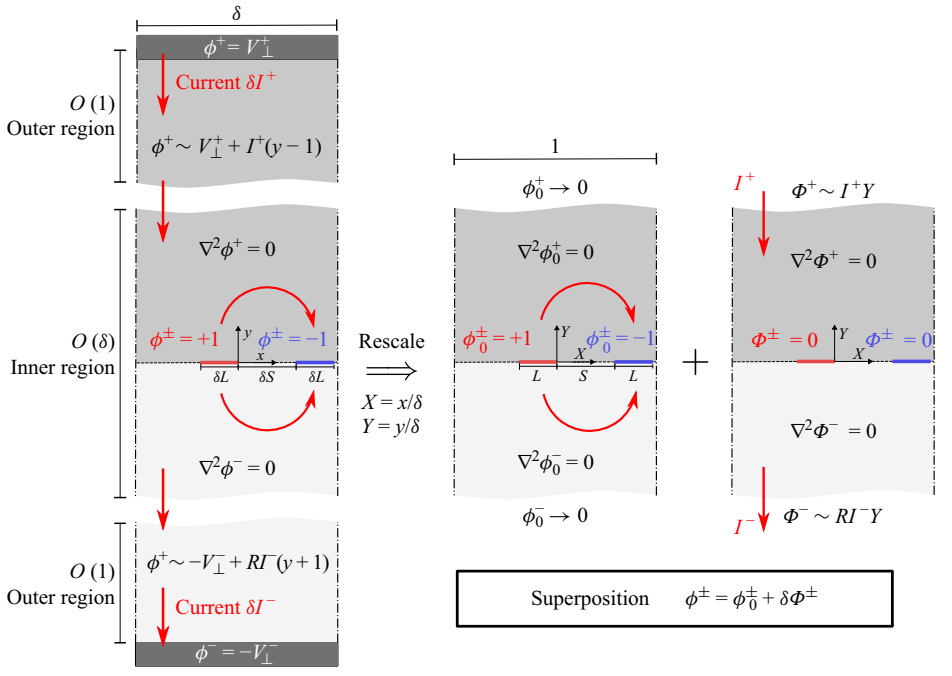


Figure 3. Schematic summarising the decomposition of the dimensionless problem for electric potentials in the limit of large channel height ($\delta \ll 1$). Inner potential problem $\phi^\pm$ shown as the superposition of $\phi_0^\pm$ (current flow between inner electrodes) and $\delta\Phi^\pm$ (disparate far-field currents). Red arrows indicate current flow. For clarity, the continuity of potentials and currents on fluid–fluid interfaces is not shown.

To consider the limit $\delta \ll 1$, it is convenient to make the domain geometry independent of the small parameter δ and transform to a new coordinate $X = x/\delta$. Henceforth, the electric Reynolds number is assumed to be zero, $Re_e = 0$.

3.1. *Outer region*

Away from the interfacial electrodes ($y = 0$), the periodic nature of the interface is not expected to be important. The governing equations in the transformed coordinate $X = x/\delta$ are written as

$$\frac{1}{\delta^2}\frac{\partial^2\phi^\pm}{\partial X^2} + \frac{\partial^2\phi^\pm}{\partial y^2} = 0, \quad \frac{1}{\delta}\frac{\partial p^\pm}{\partial X} = \frac{1}{\delta^2}\frac{\partial^2 u^\pm}{\partial X^2} + \frac{\partial^2 u^\pm}{\partial y^2}, \tag{3.1}$$

$$\frac{1}{\delta}\frac{\partial u^\pm}{\partial X} + \frac{\partial v^\pm}{\partial y} = 0, \quad \frac{\partial p^\pm}{\partial y} = \frac{1}{\delta^2}\frac{\partial^2 v^\pm}{\partial X^2} + \frac{\partial^2 v^\pm}{\partial y^2}. \tag{3.2}$$

If we then consider $\delta \ll 1$ with $y = O(1)$ (fixed), and formally expand all variables, $\phi^\pm = \phi_0^\pm + \delta\phi_1^\pm + O(\delta^2)$ etc., it can be easily shown (integrating at each order and applying periodicity in X; Hodes *et al.* 2023) that for all orders of δ, the vertical velocity is zero, and the potentials and horizontal velocity are functions of y alone. That is, $\phi_n^\pm = \phi_n^\pm(y)$, $u_n^\pm = u_n^\pm(y)$ and $v_n^\pm = 0$ (and $p_n^\pm$ constant) for all $n \geqslant 0$. Therefore, at each order, the equations are one-dimensional:

$$\frac{\mathrm{d}^2\phi_n^\pm}{\mathrm{d}y^2} = \frac{\mathrm{d}^2 u_n^\pm}{\mathrm{d}y^2} = 0. \tag{3.3}$$

https://doi.org/10.1017/jfm.2025.10499 Published online by Cambridge University Press

Integrating these, and applying the boundary conditions (2.15) and (2.21) on $y = \pm 1$ at each order, it is found that the series solutions are simply linear in y:

$$\phi^+ \sim V_\perp^+ + I^+(\delta)\,(y-1), \tag{3.4}$$

$$\phi^- \sim -V_\perp^- + RI^-(\delta)\,(y+1), \tag{3.5}$$

$$u^\pm \sim U^\pm(\delta)\,(1 \mp y), \tag{3.6}$$

$$v^\pm \sim 0, \tag{3.7}$$

where $I^\pm(\delta)$ and $U^\pm(\delta)$ are constants that depend (algebraically) on δ. The constants $I^\pm$ are the dimensionless currents (per unit area) leaving the top electrode, and entering the bottom electrode, respectively (this explains the factor R introduced in (3.5)). Also, $U^\pm(\delta)$ are the 'slip velocities' at $y = 0$, as viewed from the outer region (note that $U^+ = U^-$ here as the domain is symmetric in $y = 0$). These are determined by matching with the solution in an inner region close to the interface $y = 0$.

3.2. *Inner region*

The outer solution, depending only on y, cannot satisfy the mixed condition at the interface $y = 0$, so a different solution is needed close to the interface. Within an $O(\delta)$ distance, the diffusive terms in X will balance the diffusive terms in y, and the problem will be 2-D, but now 'unbounded' in y. An inner variable $Y = y/\delta$ is now introduced, which is taken to be $O(1)$ as $\delta \to 0$. In terms of the inner variables X and Y, the potentials and flow are governed by the full Laplace and Stokes equations (now holding for $0 < |Y| < \infty$ in each fluid):

$$\frac{\partial^2\phi^\pm}{\partial X^2} + \frac{\partial^2\phi^\pm}{\partial Y^2} = 0, \quad \frac{\partial p^\pm}{\partial X} = \frac{\partial^2 u^\pm}{\partial X^2} + \frac{\partial^2 u^\pm}{\partial Y^2}, \tag{3.8}$$

$$\frac{\partial u^\pm}{\partial X} + \frac{\partial v^\pm}{\partial Y} = 0, \quad \frac{\partial p^\pm}{\partial Y} = \frac{\partial^2 v^\pm}{\partial X^2} + \frac{\partial^2 v^\pm}{\partial Y^2}. \tag{3.9}$$

The boundary conditions at $Y = 0$ are identical to (2.10)–(2.13) and (2.17)–(2.20) but written in inner variables:

$$\phi^\pm = 1 \qquad \text{on } Y = 0, \text{ on the positive electrode } (-L < x < 0), \tag{3.10}$$

$$\phi^\pm = -1 \qquad \text{on } Y = 0, \text{ on the negative electrode } (S < x < S + L), \tag{3.11}$$

$$\phi^+ = \phi^- \qquad \text{on } Y = 0, \text{ on the menisci}, \tag{3.12}$$

$$R\frac{\partial\phi^+}{\partial Y} - \frac{\partial\phi^-}{\partial Y} = 0 \qquad \text{on } Y = 0, \text{ on the menisci}, \tag{3.13}$$

and

$$\boldsymbol{u}^\pm = \boldsymbol{0} \qquad \text{on } Y = 0, \text{ on the electrodes}, \tag{3.14}$$

$$u^+ = u^- \qquad \text{on } Y = 0, \text{ on the menisci}, \tag{3.15}$$

$$v^\pm = 0 \qquad \text{on } Y = 0, \text{ on the menisci}, \tag{3.16}$$

$$m^+\frac{\partial u^+}{\partial Y} - m^-\frac{\partial u^-}{\partial Y} = q\frac{\partial\phi^+}{\partial X} \qquad \text{on } Y = 0, \text{ on the menisci}, \tag{3.17}$$

with only the expression for q differing, as

$$q = -\frac{1}{\delta}\left(\frac{\partial\phi^+}{\partial Y} - Q\frac{\partial\phi^-}{\partial Y}\right)_{Y=0} = \frac{QR-1}{\delta}\left.\frac{\partial\phi^+}{\partial Y}\right|_{Y=0}. \tag{3.18}$$

https://doi.org/10.1017/jfm.2025.10499 Published online by Cambridge University Press

Note that the tangential stress condition can be replaced with

$$\frac{\partial u^+}{\partial Y} = -\frac{\partial u^-}{\partial Y} = q\frac{\partial \phi^+}{\partial X} \qquad \text{on } Y = 0, \text{ on the menisci,} \tag{3.19}$$

due to the symmetry arguments in § 2.2. Finally, there are matching conditions on this inner solution (as $Y \to \pm\infty$) with the outer solution (as $y = \delta Y \to 0$), giving

$$\phi^+ \sim V_\perp^+ + I^+(\delta)\,(\delta Y - 1), \qquad Y \to \infty, \tag{3.20}$$

$$\phi^- \sim -V_\perp^- + RI^-(\delta)\,(\delta Y + 1), \qquad Y \to -\infty, \tag{3.21}$$

$$u^\pm \sim U^\pm(\delta)\,(1 \mp \delta Y), \qquad Y \to \pm\infty, \tag{3.22}$$

$$v^\pm \to 0, \qquad Y \to \pm\infty. \tag{3.23}$$

The potential problem can be considered first, followed by the velocity field, which is driven by interfacial charge build-up. Hence the solutions for the velocity field are presented later, in § 6.

The solution to the potential problem will be presented in terms of two components: (i) the leading-order solution (corresponding to $\delta = 0$), where there is no current entering or leaving in the far field, only flowing from one interfacial electrode to the other; and (ii) a higher-order solution (accounting for all higher orders in δ), where current is entering and leaving in the far field, but with no current flowing between the interfacial electrodes themselves (although there may be net current to/from the interfacial electrodes collectively).

3.3. *Leading order: current flow between interfacial electrodes*

The case where current flows only between the two interfacial electrodes, and not into the far field, corresponds to the leading-order solution $\phi_0^\pm$, where $\delta = 0$. Then $\phi_0^\pm$ is harmonic and satisfies

$$\phi_0^\pm = 1 \quad \text{on } Y = 0, \text{ on the positive electrode } (-L < x < 0), \tag{3.24}$$

$$\phi_0^\pm = -1 \quad \text{on } Y = 0, \text{ on the negative electrode } (S < x < S + L), \tag{3.25}$$

$$\phi_0^+ = \phi_0^- \quad \text{on } Y = 0, \text{ on the menisci,} \tag{3.26}$$

$$R\frac{\partial \phi_0^+}{\partial Y} - \frac{\partial \phi_0^-}{\partial Y} = 0 \quad \text{on } Y = 0, \text{ on the menisci,} \tag{3.27}$$

$$\frac{\partial \phi_0^+}{\partial Y} - Q\frac{\partial \phi_0^-}{\partial Y} = 0 \quad \text{on } Y = 0, \text{ on the menisci.} \tag{3.28}$$

The last two conditions simplify to $\partial\phi_0^\pm/\partial Y = 0$. Finally, the matching conditions reduce to

$$\phi_0^+ \to V_\perp^+ - I_0^+, \qquad Y \to \infty, \tag{3.29}$$

$$\phi_0^- \to -V_\perp^- + RI_0^-, \qquad Y \to -\infty. \tag{3.30}$$

The problem in each individual phase ($\pm$) is identical (up to a constant multiple and shift) to one solved in Crowdy *et al.* (2023) for the thermocapillary-driven pump in the same architecture. The solution is given by (5.5)–(5.6) in § 5. Relevant here is that as $Y \to \pm\infty$, $\phi_0^\pm \to 0$, i.e. the average of the two interfacial electrode values, and this fixes the leading-order currents in the outer region(s) to be $I_0^+ = V_\perp^+$ and $RI_0^- = V_\perp^-$.

https://doi.org/10.1017/jfm.2025.10499 Published online by Cambridge University Press

3.4. *Higher order: far-field current flow past grounded interfacial electrodes*

With the leading-order potential $\phi_0^{\pm}$ known, instead of proceeding with a regular expansion in δ, seeking corrections of $O(\delta)$, and so on, here we will find a solution satisfying all orders (order δ and higher) at once. The behaviour at leading order (driven by the potential difference between the interfacial electrodes at $Y=0$) is distinct from the behaviour at higher orders (driven by a difference in current at $Y\to\pm\infty$), so we define the following perturbation potential $\Phi^{\pm}$:

$$\Phi^{\pm}=\frac{\phi^{\pm}-\phi_0^{\pm}}{\delta}. \tag{3.31}$$

Noticing that $\phi_0^{\pm}$ satisfies the inhomogeneous conditions on the electrodes at $Y=0$, but otherwise satisfies homogeneous versions of all other conditions, we have that $\Phi^{\pm}$ is harmonic and satisfies

$$\Phi^{\pm}=0 \quad \text{on } Y=0, \text{ on both electrodes } (-L<x<0,\ S<x<S+L), \tag{3.32}$$

$$\Phi^{+}=\Phi^{-} \quad \text{on } Y=0, \text{ on the menisci}, \tag{3.33}$$

$$R\frac{\partial\Phi^{+}}{\partial Y}-\frac{\partial\Phi^{-}}{\partial Y}=0 \quad \text{on } Y=0, \text{ on the menisci}, \tag{3.34}$$

and now with far-field conditions

$$\Phi^{+}\sim I^{+}Y+\frac{1}{\delta}\left(V_{\perp}^{+}-I^{+}\right), \quad Y\to+\infty, \tag{3.35}$$

$$\Phi^{-}\sim I^{-}RY+\frac{1}{\delta}\left(I^{-}R-V_{\perp}^{-}\right), \quad Y\to-\infty. \tag{3.36}$$

This corresponds to the interfacial electrodes being grounded ($\Phi^{\pm}=0$), and two current densities $I^{\pm}$ at the far field. As $I^{\pm}$ are not yet known, they will differ in general, corresponding to net current flow (in some unknown proportion) between the two far fields $Y\to\pm\infty$ and the two interfacial electrodes at $Y=0$. The two-phase nature of this problem, combined with asymmetric current conditions, makes it highly non-trivial, but remarkably, a closed-form result can be found. It is derived separately in Appendix A.

The solution is given by (A46), and turns out to have the following far-field behaviour, with voltage perturbations $(I^{+}-I^{-})\Lambda$:

$$\Phi^{+}\sim I^{+}Y+(I^{+}-I^{-})\Lambda, \quad Y\to+\infty, \tag{3.37}$$

$$\Phi^{-}\sim I^{-}RY+(I^{+}-I^{-})\Lambda, \quad Y\to-\infty, \tag{3.38}$$

where Λ is a constant known from the geometry, given by (4.9). To determine the currents $I^{\pm}$, we compare (3.35)–(3.36) with (3.37)–(3.38), giving relations

$$\frac{1}{\delta}\left(V_{\perp}^{+}-I^{+}\right)=(I^{+}-I^{-})\Lambda, \quad \frac{1}{\delta}\left(I^{-}R-V_{\perp}^{-}\right)=(I^{+}-I^{-})\Lambda, \tag{3.39}$$

which can be rearranged into the matrix equation

$$\begin{pmatrix}1+\delta\Lambda & -\delta\Lambda\\ -\delta\Lambda & R+\delta\Lambda\end{pmatrix}\begin{pmatrix}I^{+}\\ I^{-}\end{pmatrix}=\begin{pmatrix}V_{\perp}^{+}\\ V_{\perp}^{-}\end{pmatrix}, \tag{3.40}$$

involving an effective resistance matrix that depends on δ, and accounts for the combined resistance of the two phases, but also the loss (or gain) of current at the electrodes on the interface. When $\delta=0$, all of the current flows into or out of the interfacial electrodes, with

https://doi.org/10.1017/jfm.2025.10499 Published online by Cambridge University Press

no current bypassing. Inverting the above system results in

$$I^+ = \frac{(R+\delta\Lambda)V_\perp^+ + \delta\Lambda V_\perp^-}{R+(R+1)\delta\Lambda}, \tag{3.41}$$

$$I^- = \frac{\delta\Lambda V_\perp^+ + (1+\delta\Lambda)V_\perp^-}{R+(R+1)\delta\Lambda}. \tag{3.42}$$

With $I^\pm$ determined as above, the full inner solution is

$$\phi^\pm \sim \phi_0^\pm(X,Y) + \delta\,\Phi^\pm(X,Y;I^+,I^-), \quad Y = y/\delta = O(1), \quad \delta \to 0. \tag{3.43}$$

3.4.1. *Special case: $I^+ = I^-$*

We remark about a special case where, for a particular choice of lower potential $V_\perp^- = V_\perp^+ R$, the above collapses to $I^+ = I^- = V_\perp^+$, and the $\Phi^\pm$ solutions are trivial linear functions of Y, i.e. the current flowing between the upper and lower electrodes does not interact mathematically with the interfacial electrodes. Physically, this case corresponds to one where no net current is generated by the inner electrodes so that the currents at the top and the bottom of the domain are identical. Importantly, this does not mean that no current from the far field flows into the inner electrodes, but exactly the same flows in as flows out. This case is discussed in more detail later in the paper, including visualisation.

3.4.2. *Composite potential solution*

Remarkably, the above solution (3.43) (when substituting for outer variables $(X,Y) = (x/\delta, y/\delta)$) is also the composite solution, uniformly valid for all $-1 < y < 1$. This is because (3.43) becomes precisely the outer solution to all orders if expanded for $Y = y/\delta \to \pm\infty$.

4. Solution for far-field current flow past interfacial electrodes

This section summarises the solution to the unbounded two-phase potential problem, where the far-field currents in both phases are in general different, and the interfacial electrodes are grounded. This appears as one component of the inner solution, close to the interface $y = 0$, embedded within a finite channel as described in § 3. However, since it is non-trivial and will also likely have applications in other contexts, a detailed derivation is given in Appendix A.

The solution is given in terms of complex potentials

$$w^+(z) = \Phi^+ + \mathrm{i}\chi^+, \quad w^-(z) = \Phi^- + \mathrm{i}\chi^-, \quad \text{where } z = X + \mathrm{i}Y, \tag{4.1}$$

in the upper (+) and lower (−) period semi-strips. The conformal mapping function

$$z = Z(\zeta) = -\frac{\mathrm{i}}{2\pi}\log\eta(\zeta), \tag{4.2}$$

where

$$\eta(\zeta) = M\frac{P(\zeta/\alpha,\rho)\,P(\zeta\alpha,\rho)}{P(\zeta/\overline{\alpha},\rho)\,P(\zeta\overline{\alpha},\rho)}, \quad P(\zeta,\rho) = (1-\zeta)\prod_{n=1}^{\infty}(1-\rho^{2n}\zeta)(1-\rho^{2n}/\zeta), \tag{4.3}$$

with $\alpha = \mathrm{i}r$ for $\rho < r < 1$, transplants the upper half-annulus

$$\rho < |\zeta| < 1, \quad \mathrm{Im}[\zeta] \geqslant 0, \tag{4.4}$$

to the upper half-period strip – see Appendix A for full details.

https://doi.org/10.1017/jfm.2025.10499 Published online by Cambridge University Press

The two-phase solution in this auxiliary ζ annulus is found to be

$$w^+(z) = W^+(\zeta) = -\frac{R}{R+1}\left[\frac{I^+ + RI^-}{2\pi R}\log\eta(\zeta) + \frac{I^+ - I^-}{2\pi}\log\xi(\zeta)\right],$$
$$w^-(z) = W^-(\zeta) = -\frac{R}{R+1}\left[\frac{I^+ + RI^-}{2\pi}\log\eta(\zeta) - \frac{I^+ - I^-}{2\pi}\log\xi(\zeta)\right], \tag{4.5}$$

where

$$\xi(\zeta) = \frac{P(\zeta/\alpha,\,\rho)\,P(\zeta\overline{\alpha},\,\rho)}{P(\zeta/\overline{\alpha},\,\rho)\,P(\zeta\alpha,\,\rho)}. \tag{4.6}$$

The required potentials $\Phi^\pm$ then follow as the real parts of the above functions $w^\pm$.

When $I^- = I^+$, these formulas reduce to the trivial linear solutions

$$w^+(z) = -\mathrm{i}I^+ z, \quad w^-(z) = -\mathrm{i}RI^- z, \tag{4.7}$$

as expected.

It can also be shown that the far-field behaviours (real part of (4.5) as $Y \to \pm\infty$) are

$$\Phi^+ \sim I^+ Y + (I^+ - I^-)\Lambda, \quad \Phi^- \sim RI^- Y + (I^+ - I^-)\Lambda, \tag{4.8}$$

where

$$\Lambda = \frac{R}{\pi(R+1)}\log\left|\frac{P(\alpha^2,\,\rho)}{P(|\alpha|^2,\,\rho)}\right|. \tag{4.9}$$

The constants α and ρ are easily found (Appendix A) as part of the conformal map for use in the above formulas, and they depend only on the geometry.

5. Solution for current flow between interfacial electrodes

The solution for the separate case where the two interfacial electrodes are held at constant potentials $+1$ and -1, with no current entering/leaving in the far field, is also a relevant component of the solution close to the interface (it is the problem for $\phi_0^\pm$ in § 3.3). It utilises the same conformal map (A7), and relies on a solution from Crowdy *et al.* (2023).

Notice that the boundary conditions (3.26)–(3.27) can be satisfied exactly if

$$\frac{\partial\phi_0^+}{\partial Y} = \frac{\partial\phi_0^-}{\partial Y} = 0 \quad \text{on the menisci}, \tag{5.1}$$

and we choose $\phi_0^-(X, Y) = \phi_0^+(X, -Y)$. Then the solution in the lower fluid $(-)$ is simply the reflection of that in the upper fluid $(+)$ in $Y = 0$. The problem in the $(+)$ fluid then is identical (up to a constant multiple and shift) to one solved in Crowdy *et al.* (2023) for a thermocapillary-driven pump in the same architecture where the electrodes in the present problem are hot/cold 'ridges' in the thermocapillary-driven pump. Let T be the temperature field solution from Crowdy *et al.* (2023) where one ridge is at temperature $T = 1$ and the other is at $T = 0$. Then the solution here for the potential ϕ_0^+ is given by $\phi_0^+ = 2T - 1$.

Writing the complex potentials in the two phases as

$$w_0^\pm(z) = \phi_0^\pm + \mathrm{i}\psi_0^\pm, \tag{5.2}$$

https://doi.org/10.1017/jfm.2025.10499 Published online by Cambridge University Press

the solution $w_0^+(Z(\zeta)) = W_0^+(\zeta)$ in the upper ζ annulus under map (A7) is simply (Crowdy *et al.* 2023)

$$W_0^+(\zeta) = 1 + \frac{2\mathrm{i}}{\pi}\log\zeta, \tag{5.3}$$

and by symmetry, the solution $w_0^-(Z(\zeta)) = W_0^-(\zeta)$ in the lower annulus is also

$$W_0^-(\zeta) = 1 - \frac{2\mathrm{i}}{\pi}\log\zeta. \tag{5.4}$$

Taking the real parts yields the potentials $\phi_0^\pm$:

$$\phi_0^+ = 1 - \frac{2}{\pi}\arg\zeta, \tag{5.5}$$

$$\phi_0^- = 1 + \frac{2}{\pi}\arg\zeta. \tag{5.6}$$

In the far field, it turns out that $\zeta \to \alpha$ and $\zeta \to \bar{\alpha}$, which have arguments $+\pi/2$ and $-\pi/2$, respectively, leading to $\phi_0^\pm \to 0$, as expected.

6. Induced velocity

If the potential fields $\phi^\pm$ are known, as detailed in §§ 3–5, then the flow velocity, induced by the interfacial Maxwell stress, can now be calculated. It is sufficient to focus on the flow in the inner region close to the interface, since the solution in the outer region is simple, given by (3.6). The equations governing the flow in the inner region are given by (3.8)–(3.9), (3.14)–(3.18), (3.22)–(3.23).

First, the surface charge accumulated on the menisci is given by (3.18). Substituting the asymptotic solution (3.43) for the potentials and noting that $\partial\phi_0^+/\partial Y = 0$ on the menisci, we find

$$q = (QR - 1)\left.\frac{\partial\Phi^+}{\partial Y}\right|_{Y=0}. \tag{6.1}$$

We remark that it was shown earlier, in § 2.2, that the velocity fields in both fluids are the same, surprisingly, up to reflection in $y = 0$, so it is sufficient to solve for $\boldsymbol{u}^+$ only, with meniscus condition (3.19). It is convenient in the complex variable formation to consider both $\boldsymbol{u}^\pm$ simultaneously. Substituting q into the stress balance (3.19) on the menisci, the flow fields can be resolved. We introduce the streamfunctions $\psi^\pm$,

$$u^\pm = \frac{\partial\psi^\pm}{\partial Y}, \quad v^\pm = -\frac{\partial\psi^\pm}{\partial X}, \tag{6.2}$$

which have the representation in the complex $z = X + \mathrm{i}Y$ plane as (Crowdy *et al.* 2023)

$$\psi^\pm = \mathrm{Im}\left[(\bar{z} - z)\, f^\pm(z)\right], \tag{6.3}$$

where $f^\pm(z)$ are analytic functions in the upper and lower domains, respectively. It can be easily shown that $u^\pm - \mathrm{i}v^\pm = -2\,\mathrm{Re}[f^\pm(z)] + (\bar{z} - z)(f^\pm(z))'$, from which the far-field behaviours (3.22)–(3.23) imply conditions on $f^\pm(z)$:

$$f^+(z) \sim -\frac{1}{2}U^+ + \mathrm{i}c - \frac{1}{4}\delta U^+\mathrm{i}z \quad \text{as } z \to \infty,\ \mathrm{Im}[z] > 0, \tag{6.4}$$

$$f^-(z) \sim -\frac{1}{2}U^- + \mathrm{i}c + \frac{1}{4}\delta U^-\mathrm{i}z \quad \text{as } z \to \infty,\ \mathrm{Im}[z] < 0, \tag{6.5}$$

https://doi.org/10.1017/jfm.2025.10499 Published online by Cambridge University Press

for some inconsequential imaginary constant ic. From symmetry (§ 2.2), we must have $U^+ = U^- =: U$. An implication of the complex representation is that (Crowdy *et al.* 2023)

$$u^{\pm} = -2\,\mathrm{Re}[f^{\pm}(z)] \quad \text{on } Y = 0, \tag{6.6}$$

which means that continuity of the velocities on $Y = 0$ can be written as

$$\mathrm{Re}[f^-(z)] = \mathrm{Re}[f^+(z)] = \mathrm{Re}\big[\overline{f^+(z)}\big] = \mathrm{Re}\big[\overline{f^+}(z)\big] \quad \text{on } Y = 0, \tag{6.7}$$

where the Schwarz conjugate function $\overline{f}(z)$ is defined as $\overline{f}(z) = \overline{f(\overline{z})}$. An important observation is that if $f(z)$ is upper analytic, then $\overline{f}(z)$ is lower analytic with the same far-field behaviour. The up–down flow symmetry in the plane $Y = 0$ can be expressed here as $f^-(z) = \overline{f^+}(z)$. And the tangential stress condition (3.19) for u^+ can be written, using that $\partial u^{\pm}/\partial Y = \partial(-2\,\mathrm{Im}[f^{\pm}(z)])/\partial X$ on $Y = 0$, as

$$\frac{\partial}{\partial X}\left(-2\mathrm{Im}[f^+(z)]\right) = q\frac{\partial \phi^+}{\partial X} \quad \text{on } Y = 0, \text{ on the menisci.} \tag{6.8}$$

6.1. *Pumping speed formula from reciprocity*

In general, solution of the inner velocity field with Maxwell stress forcing is somewhat difficult. However, due to the form of the outer solutions in (3.6) and (3.7), the key parameters of interest are the effective slip velocities $U^{\pm}$ (which are identical by symmetry, and denoted by U). Therefore, we can focus on solving for U, which can be done using reciprocal theorem arguments, without the need to resolve the full velocity field.

Lorentz reciprocity holds, on some domain D given our solution $\{u_i^+, \sigma_{ij}^+\}$ and an auxiliary solution $\{\hat{u}_i, \hat{\sigma}_{ij}\}$, that

$$\oint_{\partial D} u_i^+ \hat{\sigma}_{ij} n_j \,\mathrm{d}l = \oint_{\partial D} \hat{u}_i \sigma_{ij}^+ n_j \,\mathrm{d}l, \tag{6.9}$$

where σ_{ij} denotes a hydrodynamic stress tensor. To calculate U, it is sufficient to choose the domain to be the upper periodic domain (semi-strip) and define the auxiliary solution to be that of a shear flow over an arbitrary array of unequal no-shear menisci between transverse electrodes as solved by Crowdy (2011). Crucially, it has the behaviour

$$\hat{u} \sim Y + \lambda_\perp \quad \text{as } Y \to \infty, \tag{6.10}$$

where

$$\lambda_\perp = \frac{1}{\pi}\log\left|\frac{P(\alpha^2, \rho)}{P(|\alpha|^2, \rho)}\right| \tag{6.11}$$

is the hydrodynamic slip length (notice the similarity to (4.9) mentioned earlier). Along solid electrodes $\hat{u}$ satisfies no-slip conditions, and along the two menisci it satisfies no-shear conditions.

On the left-hand side of (6.9), the only term that is non-zero is at the boundary at $Y = \infty$. Conversely, on the right-hand side, the $Y = \infty$ term and terms along both menisci are non-zero. The result is

$$\begin{aligned}\int_{-1/2}^{1/2} U\,(1 - \delta Y)\,\mathrm{d}X = &\int_{-1/2}^{1/2} -\delta U\,(Y + \lambda_\perp)\,\mathrm{d}X \\ &- \int_{men\ 1} \hat{u}\frac{\partial u^+}{\partial Y}\,\mathrm{d}X - \int_{men\ 2} \hat{u}\frac{\partial u^+}{\partial Y}\,\mathrm{d}X.\end{aligned} \tag{6.12}$$

https://doi.org/10.1017/jfm.2025.10499 Published online by Cambridge University Press

The first two integrals can be directly evaluated, and the equation rearranged to give

$$U = -\frac{1}{1+\delta\lambda_\perp}\left[\int_{men\ 1} \hat{u}q\frac{\partial\phi^+}{\partial X}\,\mathrm{d}X + \int_{men\ 2} \hat{u}q\frac{\partial\phi^+}{\partial X}\,\mathrm{d}X\right], \tag{6.13}$$

where we have applied (3.19). Substituting (6.1) for q and (3.43) for ϕ^+ gives

$$U = -\frac{QR-1}{1+\delta\lambda_\perp} \times\left[\int_{men\ 1} \hat{u}\frac{\partial\Phi^+}{\partial Y}\left(\frac{\partial\phi_0^+}{\partial X}+\delta\frac{\partial\Phi^+}{\partial X}\right)\mathrm{d}X + \int_{men\ 2} \hat{u}\frac{\partial\Phi^+}{\partial Y}\left(\frac{\partial\phi_0^+}{\partial X}+\delta\frac{\partial\Phi^+}{\partial X}\right)\mathrm{d}X\right]. \tag{6.14}$$

After using one of the Cauchy–Riemann equations to replace Y derivatives, it follows that

$$U = \frac{QR-1}{1+\delta\lambda_\perp} \times\left[\int_{men\ 1} \hat{u}\frac{\partial\chi^+}{\partial X}\left(\frac{\partial\phi_0^+}{\partial X}+\delta\frac{\partial\Phi^+}{\partial X}\right)\mathrm{d}X + \int_{men\ 2} \hat{u}\frac{\partial\chi^+}{\partial X}\left(\frac{\partial\phi_0^+}{\partial X}+\delta\frac{\partial\Phi^+}{\partial X}\right)\mathrm{d}X\right], \tag{6.15}$$

which must be evaluated numerically, but this is easily done. Note that all derivatives are in X, so knowledge of the functions on the interfaces is all that is required to evaluate the integrand.

6.2. *Special case:* $V_\perp^- = RV_\perp^+$

The special case (shown later to be the case for optimal pumping speed) where the upper/lower electrode values satisfy $V_\perp^- = RV_\perp^+$, and hence the currents leaving the upper and entering the lower electrodes are equal ($I^+ = I^-$), simplifies considerably. In this case, Φ^+ simplifies to a linear function of Y, and $I^+ = V_\perp^+$:

$$\Phi^+ = V_\perp^+ Y. \tag{6.16}$$

Thus (6.14) reduces to

$$U = -\frac{(QR-1)V_\perp^+}{1+\delta\lambda_\perp}\left[\int_{men\ 1} \hat{u}\frac{\partial\phi_0^+}{\partial X}\,\mathrm{d}X + \int_{men\ 2} \hat{u}\frac{\partial\phi_0^+}{\partial X}\,\mathrm{d}X\right]. \tag{6.17}$$

The flow $\hat{u}$ is known from Crowdy (2011), and on $Y=0$, it can be expressed as $\hat{u} = -2\,\mathrm{Re}[\hat{f}(z)]$, where, in the ζ annulus,

$$\hat{f}(z) = \hat{f}(Z(\zeta)) = \frac{1}{8\pi}\log\xi(\zeta), \tag{6.18}$$

$$\hat{u} = -\frac{1}{4\pi}\log|\xi(\zeta)| = -\frac{1}{4\pi}\log\left|\frac{P(\zeta/\alpha,\rho)\,P(\zeta\bar{\alpha},\rho)}{P(\zeta/\bar{\alpha},\rho)\,P(\zeta\alpha,\rho)}\right|, \quad \zeta \text{ on } C_0^+, C_1^+, \tag{6.19}$$

where C_0^+, C_1^+ are upper half-circles representing the preimages of the menisci in the ζ plane – see figure 14 below. (The same function $\hat{f}(z)$ is stated with the incorrect sign in (63) of Crowdy *et al.* (2023). However, the final pumping speed formulas reported there are correctly stated.) On either meniscus, ψ_0^+ is constant, so $\mathrm{d}\phi_0^+ = \mathrm{d}W_0^+ = 2\mathrm{i}\,\mathrm{d}\zeta/(\pi\zeta)$

https://doi.org/10.1017/jfm.2025.10499 Published online by Cambridge University Press

from (5.3). Putting these elements together, (6.17) becomes

$$U = \frac{2(QR-1)V_\perp^+}{1+\delta\lambda_\perp}\left(-\frac{1}{4\pi^2}\right)\left(\int_{C_0^+} - \int_{C_1^+}\right)\log\left|\frac{P(\zeta/\alpha,\,\rho)\,P(\zeta\bar{\alpha},\,\rho)}{P(\zeta/\bar{\alpha},\,\rho)\,P(\zeta\alpha,\,\rho)}\right|\frac{\mathrm{d}\zeta}{\mathrm{i}\zeta}, \tag{6.20}$$

where C_0^+ and C_1^+ are traversed anticlockwise. It is also noted that for this special case $V_\perp^- = RV_\perp^+$, the detailed velocity field can be found throughout the domain since the Maxwell stress becomes identical, up to scaling factors, to the Marangoni stress determined in Crowdy *et al.* (2023). The solution in Crowdy *et al.* (2023) has no linear component, and corresponds here to the quantity $f^+(z) + \delta U\mathrm{i}z/4$, so the function $f^+(z)$ giving the streamfunction (6.3) has the series representation

$$f^+(z) = \frac{\mathrm{i}(QR-1)V_\perp^+}{2(1+\delta\lambda_\perp)}\left[\frac{1}{2} + \sum_{n\geqslant 1}\frac{2}{1+\rho^n}\left(\frac{1-(-1)^n}{(\pi n)^2}\right)\left(\zeta^n + \frac{\rho^n}{\zeta^n}\right)\right] - \frac{\delta U}{4}\mathrm{i}z. \tag{6.21}$$

From this analytical solution, and recalling that $u - \mathrm{i}v = -2\,\mathrm{Re}[f^+]$, the far-field velocity can simply be evaluated at $\zeta = \alpha$, yielding a second expression for U given by

$$U = \frac{(QR-1)V_\perp^+}{(1+\delta\lambda_\perp)}\,\mathrm{Im}\left[\sum_{n\geqslant 1}^{\infty}\frac{2}{1+\rho^n}\left(\frac{1-(-1)^n}{(\pi n)^2}\right)\left(\alpha^n + \frac{\rho^n}{\alpha^n}\right)\right]. \tag{6.22}$$

This can be further manipulated, on use of $\alpha = \mathrm{i}r$, to give

$$U = \frac{4(QR-1)V_\perp^+}{\pi^2(1+\delta\lambda_\perp)}\left[\sum_{m\geqslant 1}^{\infty}\frac{(-1)^{m+1}}{(2m-1)^2(1+\rho^{2m-1})}\left(r^{2m-1} - \left(\frac{\rho}{r}\right)^{2m-1}\right)\right]. \tag{6.23}$$

7. Currents and power

Some quantities of interest to the operation of the pump are (i) the total current flowing between each of the electrodes, and hence (ii) the electrical power requirement. Given a choice of electrode potentials, the current follows from integrals of the solution.

7.1. *Current flow from interfacial electrodes*

We are interested in the dimensionless current (per unit depth) entering (or leaving) from the high and low electrodes at the interface. The direct way to calculate this is by integrating the current density entering both fluids from a given interfacial electrode. For the high electrode, referred to here as 'electrode 1' (where $\phi^\pm = +1$), this is

$$I_1 = \int_{electrode\ 1}\left[-\frac{\partial\phi^+}{\partial Y} + \frac{1}{R}\frac{\partial\phi^-}{\partial Y}\right]\mathrm{d}X. \tag{7.1}$$

However, we can substitute solution (3.43) for $\phi^\pm$:

$$I_1 = \int_{electrode\ 1}\left[-\left(\frac{\partial\phi_0^+}{\partial Y} + \delta\frac{\partial\Phi^+}{\partial Y}\right) + \frac{1}{R}\left(\frac{\partial\phi_0^-}{\partial Y} + \delta\frac{\partial\Phi^-}{\partial Y}\right)\right]\mathrm{d}X \tag{7.2}$$

$$= -\int_{electrode\ 1}\left[\left(\frac{\partial\phi_0^+}{\partial Y} - \frac{1}{R}\frac{\partial\phi_0^-}{\partial Y}\right) + \delta\left(\frac{\partial\Phi^+}{\partial Y} - \frac{1}{R}\frac{\partial\Phi^-}{\partial Y}\right)\right]\mathrm{d}X. \tag{7.3}$$

https://doi.org/10.1017/jfm.2025.10499 Published online by Cambridge University Press

Then, using $\partial\phi_0^-/\partial Y = -\partial\phi_0^+/\partial Y$ (the same does not hold for $\Phi^\pm$) and the Cauchy–Riemann equations,

$$I_1 = \int_{electrode\ 1} \left[\left(1 + \frac{1}{R}\right) \frac{\partial \psi_0^+}{\partial X} + \delta \left(\frac{\partial \chi^+}{\partial X} - \frac{1}{R} \frac{\partial \chi^-}{\partial X} \right) \right] \mathrm{d}X, \tag{7.4}$$

which can readily be integrated and evaluated at the edges of the electrode:

$$I_1 = \left[\left(1 + \frac{1}{R}\right) \psi_0^+ \right]_{electrode\ 1} + \delta \left[\chi^+ - \frac{1}{R}\chi^- \right]_{electrode\ 1}, \tag{7.5}$$

where $[\cdot]$ denotes the jump across the electrode, from right to left.

The same can be done for the second interfacial electrode, or 'electrode 2' (where $\phi^\pm = -1$):

$$I_2 = \left[\left(1 + \frac{1}{R}\right) \psi_0^+ \right]_{electrode\ 2} + \delta \left[\chi^+ - \frac{1}{R}\chi^- \right]_{electrode\ 2}. \tag{7.6}$$

For the first term: taking the imaginary part of solution (5.3) gives ψ_0^+, and evaluating at the electrode edges ($\zeta = \rho$ and 1 for electrode 1, and $\zeta = -1$ and $-\rho$ for electrode 2) and taking the difference gives simply $\pm(2/\pi)\log(1/\rho)$. In addition, it is shown in (A6) that $\chi^+ - \chi^-/R$ is constant on the menisci (where the fluids are in contact), taking different constant values (c_1 and c_2) on the different menisci (1 and 2). From the arrangement shown in figure 14 below, and the fact that $\chi^\pm$ is continuous at electrode edges, we have

$$\left[\chi^+ - \frac{1}{R}\chi^- \right]_{electrode\ 1} = c_1 - c_2 = (I^- - I^+)/2, \tag{7.7}$$

since we chose $c_2 = 0$, and c_1 followed from the solution. The electrodes can be interchanged in the problem for $\Phi^\pm$ (as they both appear grounded, at the same potential), thus the current out of both electrodes for that case must be the same, hence (7.7) holds for electrode 2 also. Putting these results together, expressions for I_1 and I_2 are

$$I_1 = +\left(1 + \frac{1}{R}\right) \frac{2}{\pi} \log(1/\rho) + \delta \frac{I^- - I^+}{2}, \tag{7.8}$$

$$I_2 = -\left(1 + \frac{1}{R}\right) \frac{2}{\pi} \log(1/\rho) + \delta \frac{I^- - I^+}{2}. \tag{7.9}$$

To interpret the terms in each expression, consider the sum and (half the) difference of I_1 and I_2:

$$I_1 + I_2 = \delta(I^- - I^+), \quad \frac{I_1 - I_2}{2} = \left(1 + \frac{1}{R}\right) \frac{2}{\pi} \log(1/\rho). \tag{7.10}$$

The first equation is a statement that the combined total current entering the fluid via the two interfacial electrodes must balance the current leaving via the upper and lower electrodes, and hence is expected from a global current balance. Then the second equation is a measure of the current flowing from interfacial electrode 1 to interfacial electrode 2 (the factor $1 + 1/R$ accounting for the fact that the current can travel through both fluids). Hence the currents (7.8)–(7.9) can be clearly seen as a superposition of these two components.

https://doi.org/10.1017/jfm.2025.10499 Published online by Cambridge University Press

7.2. *Power*

From these currents, we can evaluate the electric power required to operate the pump. There are four electrodes per period, hence four sources or sinks of current, with six independent pathways for current to flow. The current could: flow from one inner electrode to the other (path 1); flow from the top electrode to either inner electrode (paths 2 and 3); flow from either inner electrode to the bottom electrode (paths 4 and 5); flow directly from the top electrode to the bottom electrode (path 6).

Power density can be defined locally in the upper and lower domains as

$$\boldsymbol{P}^+ = -\phi^+ \nabla\phi^+ \quad \text{and} \quad \boldsymbol{P}^- = -\frac{1}{R}\phi^- \nabla\phi^-, \tag{7.11}$$

respectively. To calculate the total power (per unit depth) input to operate the pump, we need to integrate the (inward) normal component along the boundaries. In the upper and lower domains, this becomes (where $\boldsymbol{n}$ is the inward normal in each case)

$$P^+_{in} = \oint_{upper\,fluid} \boldsymbol{P}^+ \cdot \boldsymbol{n}\, \mathrm{d}l = \int_{y=1} V^+_\perp \frac{\partial\phi^+}{\partial y}\, \mathrm{d}x + \int_{y=0} -\phi^+ \frac{\partial\phi^+}{\partial y}\, \mathrm{d}x \tag{7.12}$$

$$= \delta V^+_\perp I^+ - \int_{-1/2}^{1/2} \phi^+ \frac{\partial\phi^+}{\partial Y}\bigg|_{Y=0} \mathrm{d}X, \tag{7.13}$$

$$P^-_{in} = \oint_{lower\,fluid} \boldsymbol{P}^- \cdot \boldsymbol{n}\, \mathrm{d}l = -\int_{y=-1} \frac{-V^-_\perp}{R} \frac{\partial\phi^-}{\partial y}\, \mathrm{d}x + \int_{y=1} \frac{\phi^-}{R} \frac{\partial\phi^-}{\partial y}\, \mathrm{d}x \tag{7.14}$$

$$= \delta V^-_\perp I^- + \frac{1}{R}\int_{-1/2}^{1/2} \phi^- \frac{\partial\phi^-}{\partial Y}\bigg|_{Y=0} \mathrm{d}X, \tag{7.15}$$

since the only non-zero power flux is at the interface $y = 0$ or the top and bottom, $y = \pm 1$. The integrals along the interface are written in terms of inner variables.

Adding together P^+_{in} and P^-_{in} leads to the total power in, P_{in}. We can use that potentials and currents (and hence power flux) are continuous across fluid–fluid portions of $Y = 0$, and on the electrode portions we have constant potentials, so the total power is

$$P_{in} = \delta\left(I^+ V^+_\perp + I^- V^-_\perp\right) + \int_{electrode\ 1} \left[-\frac{\partial\phi^+}{\partial Y} + \frac{1}{R}\frac{\partial\phi^-}{\partial Y}\right] \mathrm{d}X$$
$$- \int_{electrode\ 2} \left[-\frac{\partial\phi^+}{\partial Y} + \frac{1}{R}\frac{\partial\phi^-}{\partial Y}\right] \mathrm{d}X = \delta(I^+ V^+_\perp + I^- V^-_\perp) + I_1 - I_2, \tag{7.16}$$

where I_1, I_2 are the currents leaving the interfacial electrodes.

Using our asymptotic solution, $I_1 - I_2$ is simply twice the current flowing between interfacial electrodes, given by (7.10). And I^+, I^- are given by (3.41)–(3.42).

7.3. *Efficiency*

One measure of the performance of the pump is the efficiency, which we define here as the ratio of the output power to the input power. The input power P_{in} is given by (7.16). The output power corresponds here to the rate of work done by the interfacial driving stresses on the fluid. This can be calculated from our solution most easily from the outer solution (3.6) as $y \to 0$. (Note that this neglects some small losses due to viscous dissipation in the inner region, which are higher order in δ.) For the (+) fluid, the rate

https://doi.org/10.1017/jfm.2025.10499 Published online by Cambridge University Press

of work here is velocity U times shear stress $-m^+\,\partial u^+/\partial y = m^+U$, integrated over one period:

$$P^+_{out} = \int_{period} U\left(-m^+\frac{\partial u^+}{\partial y}\right)_{y=0} \mathrm{d}x \sim \delta m^+ U^2. \tag{7.17}$$

Similarly for the lower fluid, $P^-_{out} \sim \delta m^- U^2$, hence the total output power to both fluids, $P_{out} = P^+_{out} + P^-_{out}$, is simply (using that $m^+ + m^- = 1$)

$$P_{out} \sim \delta U^2. \tag{7.18}$$

This output power is dimensionless, and it corresponds to a dimensional power (using the scalings in § 2)

$$P_{out,*} = (\mu^+ + \mu^-)U^2_{c*}P_{out}. \tag{7.19}$$

The corresponding dimensional input electrical power, using voltage scale $V_{\parallel *}$ and current scale $\sigma^+ V_{\parallel *}$, is

$$P_{in,*} = \sigma^+ V^2_{\parallel *} P_{in}, \tag{7.20}$$

where P_{in} is (7.16). Hence the efficiency, the ratio of output to input power, is

$$\eta_{eff} = \frac{P_{out,*}}{P_{in,*}} = \frac{Re_e}{R}\frac{P_{out}}{P_{in}} \sim \frac{Re_e}{R}\frac{\delta U^2}{P_{in}}. \tag{7.21}$$

Note that we have assumed that Re_e is small in our analysis, therefore we expect the efficiency to be low for the solutions presented here.

The above energy output is subsequently dissipated as heat via viscous dissipation. But after reaching steady state, kinetic energy has also been imparted to the fluid, totalling (per period, and per unit mass)

$$KE = \delta\int_0^1 \frac{1}{2}(u^+)^2\,\mathrm{d}y + \delta\int_{-1}^0 \frac{1}{2}(u^-)^2\,\mathrm{d}y \sim \frac{\delta U^2}{3}. \tag{7.22}$$

So even if the mechanical work is being dissipated in the present set-up, usable mechanical energy has been stored that also scales with δU^2.

8. Results

8.1. *Potential fields*

Contours of the inner variable potential fields are plotted in figures 4–6. In each figure: the leftmost plot (*a*) is the leading-order solution, capturing current flow directly from one inner electrode to the next; the middle plot (*b*) is the solution capturing the far-field current; and the rightmost plot (*c*) the combined composite solution. In each, the colours denote potential values (with solid contour lines of equipotential), the arrows indicate directions of current flow, the solid black lines at $y = 0$ represent the inner electrodes (with the leftmost being the positive one), and the dashed lines at $y = 0$ represent the flat interface between the two fluids. Across the images we have chosen geometric parameters, $S = 0.2$, $L = 0.2$ and $\delta = 0.2$ (hence the top/bottom electrodes are not pictured).

In figure 4, $R = 1/5$, $V^+_\perp = 5$, $V^-_\perp = 1$, resulting in far-field currents $I^+ \approx 10$ and $I^- \approx 5.1$, such that the inner electrodes combined act as current sinks. In figure 5, $R = 1/5$, $V^+_\perp = 5$, $V^-_\perp = 2$, resulting in far-field currents $I^+ = I^- \approx 10$, such that the inner electrodes have zero impact on the far-field currents. Finally, in figure 6, $R = 1/5$, $V^+_\perp = 5$,

https://doi.org/10.1017/jfm.2025.10499 Published online by Cambridge University Press

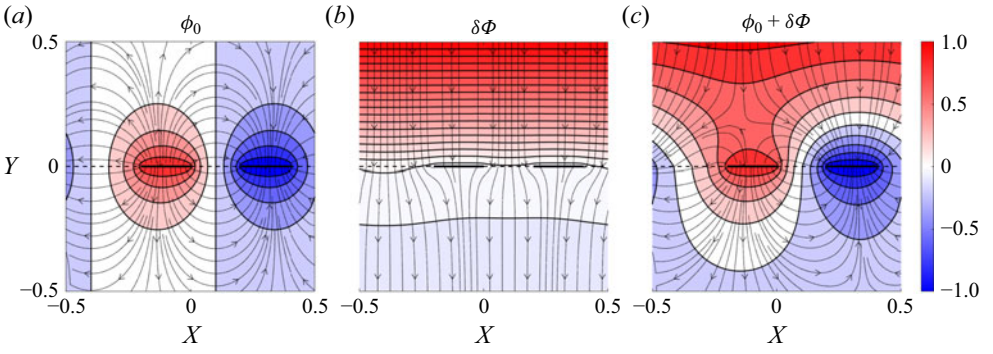


Figure 4. Contour plots of (*a*) leading-order potential, (*b*) correction to the leading order due to disparate far-field currents, and (*c*) combined full solution for the inner electric potential. In all, $R = 1/5$, $V_\perp^+ = 10$, $V_\perp^- = 1$, $S = 0.2$, $L = 0.2$ and $\delta = 0.2$. This results in far-field currents $I^+ \approx 10$ and $I^- \approx 5.1$, meaning that the inner electrodes combined act as current sinks. The solid contours (separating coloured regions) are the lines of equipotential, while the arrowed lines are everywhere tangent to current flow.

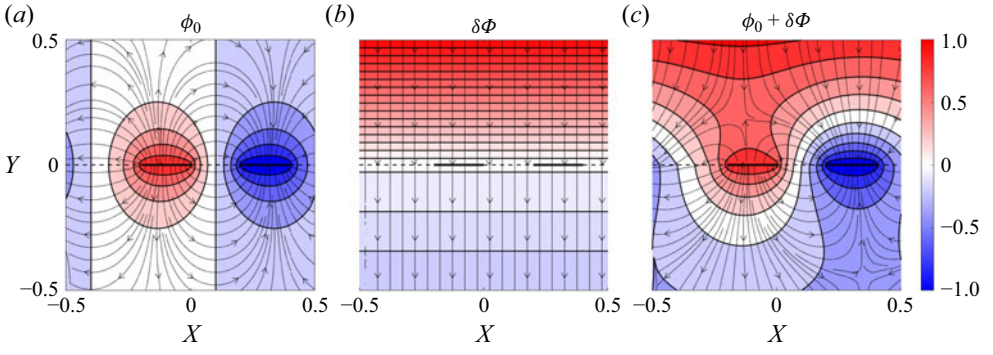


Figure 5. Contour plots of (*a*) leading-order potential, (*b*) correction to the leading order due to disparate far-field currents, and (*c*) combined full solution for the inner electric potential. In all $R = 1/5$, $V_\perp^+ = 10$, $V_\perp^- = 2$, $S = 0.2$, $L = 0.2$ and $\delta = 0.2$. This results in far-field currents $I^+ = I^- = 10$ such that the induced current is unidirectional as per (*b*). The solid contours (separating coloured regions) are the lines of equipotential, while the arrowed lines are everywhere tangent to current flow.

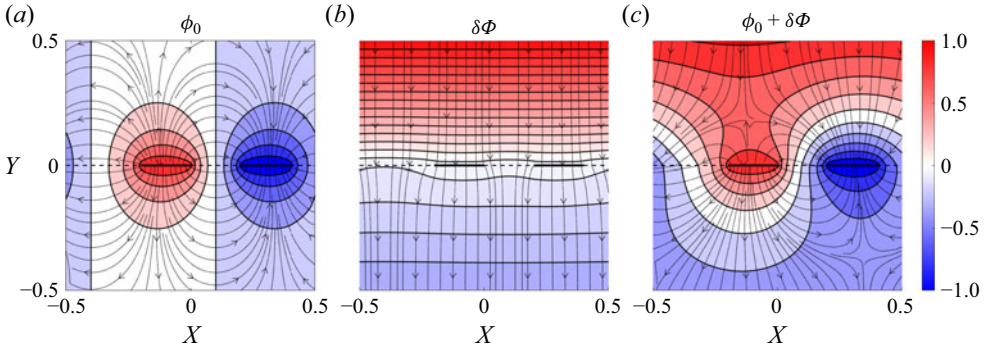


Figure 6. Contour plots of (*a*) leading-order potential, (*b*) correction to the leading order due to disparate far-field currents, and (*c*) combined full solution for the inner electric potential. In all $R = 1/5$, $V_\perp^+ = 10$, $V_\perp^- = 3$, $S = 0.2$, $L = 0.2$ and $\delta = 0.2$. This results in far-field currents $I^+ \approx 10$ and $I^- \approx 14.9$, meaning that the inner electrodes combined act as current sources. The solid contours (separating coloured regions) are the lines of equipotential, while the arrowed lines are everywhere tangent to current flow.

https://doi.org/10.1017/jfm.2025.10499 Published online by Cambridge University Press

$V_\perp^- = 3$, so that $I^+ \approx 10$ and $I^- \approx 14.9$, and the inner electrodes combined now act as current sources.

The parameter that controls whether the inner electrodes act as net sources or sinks is $RV_\perp^+ - V_\perp^-$. When this is zero, $I^+ = I^-$. When it is negative, the driving force for current flowing into the upper fluid exceeds that leaving the lower fluid, forcing the inner electrodes to collectively absorb current. Conversely, when it is positive, the opposite is true, and the inner electrodes collectively release current.

8.2. *Overall pumping ability*

We now move to a presentation of the pumping speed. In order to more conveniently compare the pumping speed across the multiple parameters, we fix the overall electrical power input of the system and solve for a relationship between $V_\perp^+$ and $V_\perp^-$. From (7.16), after substituting for I_1 and I_2, and rearranging, we have

$$I^+ V_\perp^+ + I^- V_\perp^- = \frac{1}{\delta}\left[P_{in} - \left(1 + \frac{1}{R}\right)\frac{4}{\pi}\log(1/\rho)\right], \tag{8.1}$$

where the right-hand side is determined purely by fluid properties and geometric parameters, and I^+ and I^- are given in terms of $V_\perp^\pm$ by (3.41) and (3.42), respectively. For a given $V_\perp^-$, solutions for $V_\perp^+$ can readily be obtained since this equation is quadratic in $V_\perp^+$, resulting in two solution branches,

$$V_\perp^+ = \frac{-\delta\Lambda V_\perp^- \pm \sqrt{\mathcal{M}(\rho, R)\,(\delta\Lambda + R) - [R + (1+R)\delta\Lambda]\,(V_\perp^-)^2}}{R + \delta\Lambda}, \tag{8.2}$$

where

$$\mathcal{M}(\rho, R) = \frac{1}{\delta}[R + (R+1)\delta\Lambda]\left[P_{in} - \left(1 + \frac{1}{R}\right)\frac{4}{\pi}\log(1/\rho)\right]. \tag{8.3}$$

Since R, Λ, $\mathcal{M} > 0$, real-valued solutions exist only when

$$-\sqrt{\frac{\mathcal{M}(\rho, R)\,(\delta\Lambda + R)}{R + (1+R)\delta\Lambda}} \leqslant V_\perp^- \leqslant \sqrt{\frac{\mathcal{M}(\rho, R)\,(\delta\Lambda + R)}{R + (1+R)\delta\Lambda}}. \tag{8.4}$$

To start, we fix the geometric parameters $L = S = 0.1$, $\delta = 0.2$, and the power $P_{in} = 100$, and choose $R = 1/2$ (upper fluid less conductive) and $Q = 1$. Figure 7(*a*) plots the two solution branches for $V_\perp^+$ for the range of $V_\perp^-$. The solid line is the $+$ solution branch, and the dashed line is the $-$ one.

Although the branches appear symmetric about $V_\perp^+ = 0$, there is a slight leftwards tilt caused by the term $-\delta\Lambda V_\perp^-$ in (8.2). This tilt is much clearer in figure 8(*a*), for which we have changed the geometric parameters so that $L = S = 0.01$ and $\delta = 0.5$. The remaining figure 8(*b*,*c*) show the corresponding pumping velocities (from (6.15)) and average charge on the interface(s), respectively.

In figures 7(*a–c*) and 8(*a–c*), the relationship (8.2) between the voltages takes the shape of an ellipse. Based on the signs of $V_\perp^\pm$, i.e. the quadrants of the $(V_\perp^-, V_\perp^+)$ plane in figures 7(*a*) and 8(*a*), four regions can be defined. Region I corresponds to the typical case when $V_\perp^+$, $V_\perp^- > 0$ and current is entering the domain at the top electrode and leaving at the bottom (recall that the potentials of the upper/lower electrodes are $\pm V_\perp^\pm$). Region II corresponds to when $V_\perp^+ > 0$, but $V_\perp^- < 0$, so that current is entering the domain at the top electrode and bottom electrodes, and exits entirely through the inner electrodes. Region III

https://doi.org/10.1017/jfm.2025.10499 Published online by Cambridge University Press

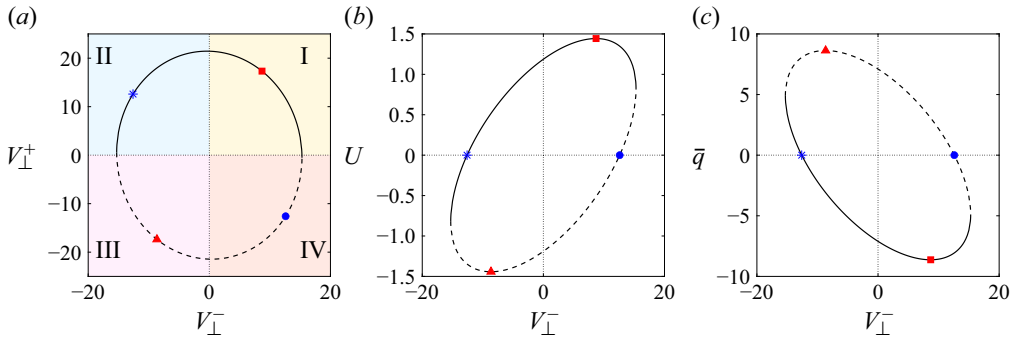


Figure 7. (*a*) Two solution branches for $V_\perp^+$, given by (8.2) for $S = 0.1$, $L = 0.1$, $\delta = 0.2$ and $R = 0.5$. Additionally, the input power is restricted to $P_{in} = 100$. (*b*) Corresponding pumping velocities for the voltage combination in (*a*). (*c*) Average charge on the two menisci. The solid lines refer to the positive solution branch, and dashed lines refer to the negative one. Markers correspond to the same solution across all panels. The blue star and circle correspond to where there is zero charge on the interfaces ($\bar{q} = 0$) and consequently the pumping speed is zero ($U = 0$). The red square and triangle correspond to the points of maximal pumping velocity in the positive and negative x directions, respectively.

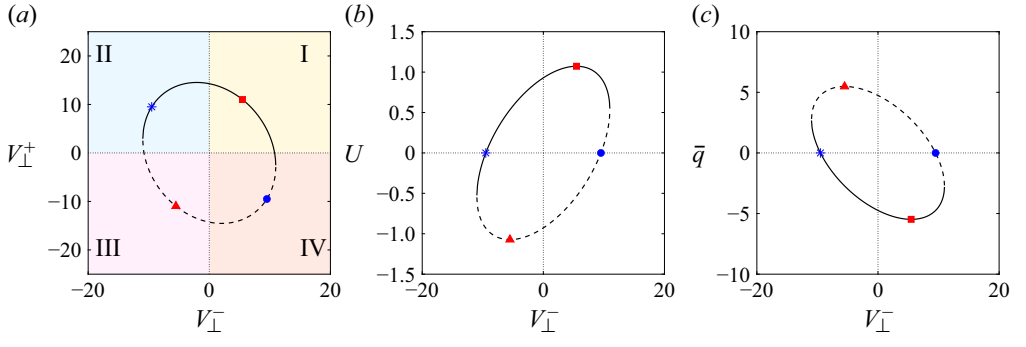


Figure 8. (a) Two solution branches for $V_\perp^+$, given by (8.2) for $S = 0.01$, $L = 0.01$, $\delta = 0.5$, $R = 0.5$ and $P_{in} = 100$. (*b*) Corresponding pumping velocities for the voltage combination in (*a*). (*c*) Average charge on the two menisci. See caption for figure 7.

corresponds to when $V_\perp^+, V_\perp^- < 0$, so that current is entering from the bottom and leaving from the top (opposite of region I). Finally, region IV corresponds to when $V_\perp^+ < 0$, but $V_\perp^- > 0$, meaning that current will leave the domain at both the top and the bottom, with all current entering through the inner electrodes (opposite of region II). In figures 7 and 8, there are four points of interest to highlight. The two blue symbols mark the cases where there is zero surface charge ($q = \bar{q} = 0$) and therefore no pumping ($U = 0$). The red symbols represent the extrema of the pumping velocity U, with the square indicating the point of maximal pumping in the x direction (thus $U > 0$), and the triangle that of maximal pumping in the $(-x)$ direction ($U < 0$). These points are marked in each panel of figures 7 and 8.

Clearly, the best pumping performance occurs when the device is in region I or III and the period-averaged current is flowing in the same direction through both fluids (either top to bottom, or bottom to top). Because far-field potential gradients point in the same direction in these cases, continuity of current allows for significant potential gradients

https://doi.org/10.1017/jfm.2025.10499 Published online by Cambridge University Press

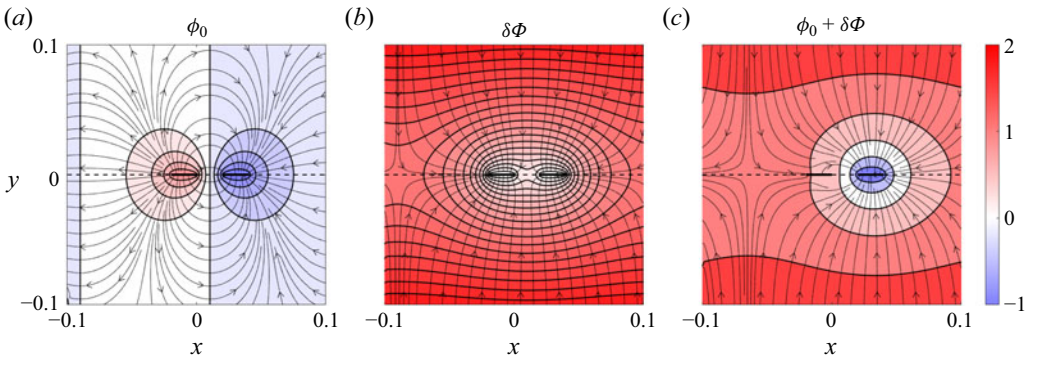


Figure 9. Contour plots of (*a*) leading-order potential, (*b*) correction to the leading order due to disparate far-field currents, and (*c*) combined full solution for the inner electric potential. Solid contours refer to lines of equipotential, and the arrowed lines are everywhere tangent to current flow. In all, $R = 1/2$, $V_\perp^+ = 12.6$, $V_\perp^- = -12.6$, $S = 0.1$, $L = 0.1$ and $\delta = 0.2$. This case leads to zero charge accumulation and fluid pumping, and corresponds to the blue star in figure 7.

at the interface. Then the jump in the electric field (really 'displacement field') between adjoining fluids allows for significant charge accumulation. Conversely, in regions II and IV, far-field potentials are of different signs, so that current is flowing either into or out of the domain at the outer electrodes, respectively. Current continuity at the interface can therefore be satisfied only if the normal interfacial gradients are close to zero, leading to very low charge build-up and hence pumping.

Notably, figures 7 and 8 both show that for these particular geometries, negative surface charge leads to pumping in the positive x direction ($U > 0$). This is because $\partial\phi^+/\partial x > 0$ along the larger meniscus. A surface Lorentz force therefore will act to drive the negative charge up the potential gradient, producing a Maxwell stress on the fluid in the positive x direction. The reverse happens on the shorter meniscus (where $\partial\phi^+/\partial x < 0$), but to a lesser extent. This difference leads to a net flow in the positive x direction.

The points of zero pumping velocity and maximal velocity magnitude are ones of interest. Zero velocity occurs when $V_\perp^+ = -V_\perp^-$, i.e. when the far-field potentials are equal (note the signs in definitions (2.15)). All current therefore must either be absorbed by or originate from the inner electrodes. Either way, the electric fields are completely symmetric about $y = 0$, and zero current crosses the menisci, leading to zero charge accumulation. To illustrate one of these cases, figure 9(*a–c*) plot the leading order, correction and full potentials, respectively, for the case of the blue star in figure 7, where $V_\perp^+ \approx 12.6$ and $V_\perp^- \approx -12.6$. It is particularly clear in figure 9(*b*) that all far-field current flows into the inner electrodes. Moreover, both the leading-order solution in figure 9(*a*) and the correction in figure 9(*b*) are symmetric about $y = 0$, thus necessitating that no current crosses this line, and precluding charge accumulation on menisci.

Conversely, maximal pumping magnitude occurs when $V_\perp^+ = (1/R)V_\perp^-$. This is the limit where zero net current flows from the far field into or out of the inner electrodes, and therefore all current that originates at one far field exits at the other ($I^+ = I^-$). This limit maximises the current flowing across menisci, which maximises the differences in the electric (or strictly displacement) fields across menisci, leading to maximal charge accumulation. Conveniently, this is also the only case in which we have obtained an analytical solution for the velocity streamfunction, given by (6.3) and (6.21). To visualise the flow pattern and the potential for this case, figure 10(*a–c*) plot streamlines for the full composite velocity field, streamlines for the flow close to the interface (inner region), and

https://doi.org/10.1017/jfm.2025.10499 Published online by Cambridge University Press

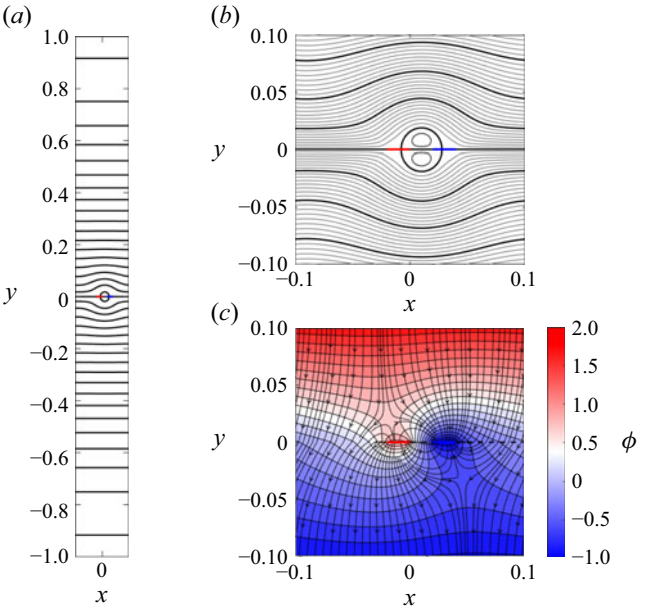


Figure 10. Plots of (*a*) velocity streamlines in the full domain, (*b*) velocity streamlines in the inner region (*a* zoomed-in perspective of (*a*)), and (*c*) contours of electric potential. In (*b*), the streamlines spacing is 8 times smaller than in (*a*), but the overlapping streamlines have been highlighted. The flow is mostly towards the right, except close to the inner electrodes where it recirculates. Here, $R = 1/2$, $V_\perp^+ \approx 17.4$, $V_\perp^- = RV_\perp^+ \approx 8.7$, $S = 0.1$, $L = 0.1$ and $\delta = 0.2$. Since the current entering at the top equals that leaving the bottom, this case leads to maximal charge accumulation and fluid pumping, and it corresponds to the red square in figure 7.

potential in the inner region, respectively. In the zoomed-in perspective of figure 10(*b*), additional streamlines have been added for visual clarity.

Figure 10(*a*) shows that the flow becomes one-dimensional relatively quickly away from the interface between the two fluids. Near the interface, the streamlines appear to bend around a region of recirculation centred on the shorter meniscus. Then in the outer region, the flow tends to a linear shear flow. Finally, figure 10(*c*) shows the electric potential.

8.3. *Effects of R and Q: conductivity and permittivity ratios*

How the scenarios of zero pumping and maximal pumping (discussed in the previous subsection) change with the conductivity ratio R can be viewed clearly in figure 11. The voltage relationships are plotted for fixed power ($P_{in} = 100$), but this time R is varied from $R = 1$ down to $R = 1/16$. The points of zero pumping remain fixed on the line $V_\perp^+ = -V_\perp^-$, while those of maximal pumping lie on the intersection of $V_\perp^+ = (1/R)V_\perp^-$ with (8.4). This intersection point, when varied with R, traces out the curve shown in figure 11(*a*). In figure 11(*a*), it is clear that decreasing R lowers the overall magnitude of both voltages. This is because decreasing R means that the lower fluid becomes more conductive. Then for the fixed potential difference (between inner electrodes), more power will flow between the inner electrodes via the lower fluid, leaving less power available for the inputs at the top and bottom electrodes. In figure 11(*b*), we plot the corresponding pumping velocities. When $R = 1$, there is zero pumping speed, hence the curve appears as a horizontal line segment on $U = 0$. When this is the case, the electric fields in the two fluids are continuous across the menisci, and since $Q = 1$ here, the displacement field is as well. Therefore no charge can accumulate. As R decreases from 1, the ellipse formed by the velocity starts to

https://doi.org/10.1017/jfm.2025.10499 Published online by Cambridge University Press

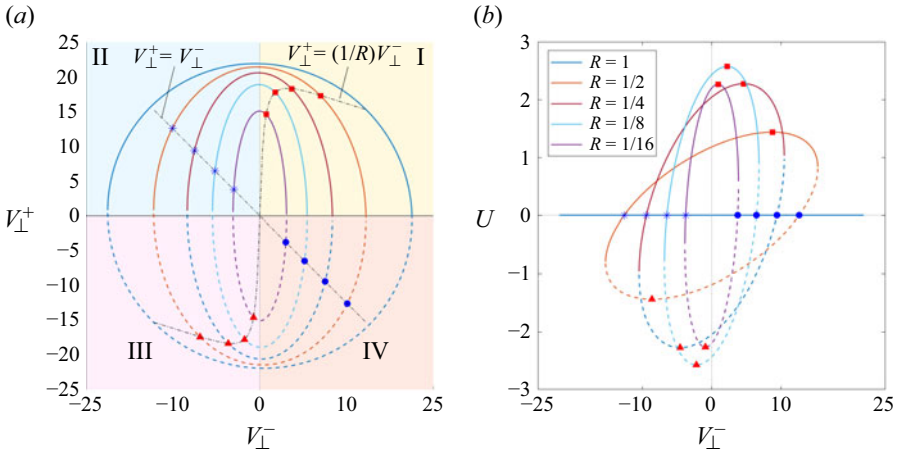


Figure 11. (*a*) Effect of varying R on two solution branches for $V_\perp^+$, given by (8.2) for $S = 0.1$, $L = 0.1$, $\delta = 0.2$ and $P_{in} = 100$. (*b*) Corresponding pumping velocities for the voltage combination in (*a*). For marker descriptions, see caption for figure 7.

orient itself to align with $V_\perp^- = 0$. This happens because as the lower fluid becomes more conductive and the overall input power is still constrained, the optimal situation becomes one where the driving potential $V_\perp^-$ and therefore the potential gradient in the lower fluid are small. Then as the potential gradient shrinks in the lower fluid, its deleterious impact on the charge accumulation is negligible, leading to more charge on the interface and more pumping. However, as R is decreased further, the power required to flow current between the two inner electrodes in the lower fluid eventually begins to dominate. This leads to a decrease in the available power to supply at the far fields, therefore smaller magnitudes of the normal electric fields.

This trend in the pumping velocity is further elucidated by figure 12, which shows how the maximum achievable velocity, at a fixed power $P_{in} = 100$, varies with R and Q. The left-hand axis is pumping velocity, while the right-hand axis is power consumed by the inner electrodes, namely $I_1 - I_2$ (see (7.16)). For reference, the $Q = 1$ curve is a continuation of the discrete maximal velocities depicted (red squares) in figure 11. The power constraint ($P_{in} = 100$) results in a minimum value of R existing; in this case, $R \gtrsim 0.033$. When $R \approx 0.033$, the inner electrodes consume all available power, with no power left to generate normal gradients in the potential fields, yielding zero charge accumulation and pumping. For all curves with $Q > 0$, the pumping speed is also zero when $QR = 1$. This is because the two fluids have identical displacement fields, therefore there is no interfacial charge accumulation. However, when $Q = 0$, the impact of the displacement field of the bottom fluid is removed entirely, and the normal potential gradient in the upper fluid is completely responsible for charge accumulation. Because the signs of the normal gradients in both fluids are the same, this maximises charge accumulation and pumping for any R, hence minimising Q would be desirable. However, even if $Q = 0$, the pumping speed decreases back to zero in the limit $R \to \infty$, as the power flowing vertically in the upper fluid vanishes, with the power flowing in the lower fluid dominating. (When $V_\perp^+ = (1/R)V_\perp^-$ is substituted into (8.2), it can be shown that $V_\perp^+ = O(R^{-1/2})$ as $R \to \infty$, but $V_\perp^- = O(R^{1/2})$. The current leaving the top electrode – the same as that entering the bottom one – is $I^+ = I^- = O(R^{-1/2})$, thus the power of the top electrode $I^+ V_\perp^+ = O(R^{-1})$ vanishes as $R \to \infty$, whereas the power of the bottom electrode, $I^- V_\perp^-$,

https://doi.org/10.1017/jfm.2025.10499 Published online by Cambridge University Press

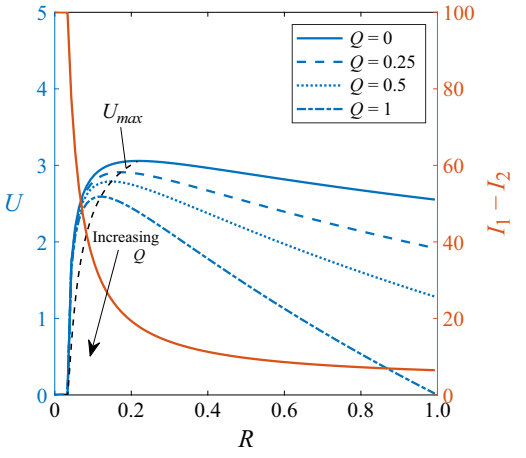


Figure 12. Left-hand axis: maximum pumping velocity (over all choices of $V_\perp^\pm$) for a fixed power input $P_{in} = 100$ as a function of R and Q. Right-hand axis: total power consumed by the inner electrodes, $I_1 - I_2$ (see (7.16)).

remains finite.) In reality if Q is small but finite, then the pumping speed will return to 0 at a finite R value, where $QR = 1$. Finally, if $QR > 1$, then the interfacial charge will become positive and the flow driven in the opposite direction, leading to negative values of U.

A direct consequence of the pumping speed approaching 0 as $R \to 0$ and $R \to \infty$ is that there exists some R that maximises the pumping speed, easily observed in figure 12. To calculate this value of R, we use (7.16) with $V_\perp^- = RV_\perp^+$ (the optimal electrode configuration) and $I^+ = I^-(= V_\perp^+)$ to write

$$V_\perp^+ = \sqrt{\frac{P_{in} - \left(1 + \dfrac{1}{R}\right)\dfrac{4}{\pi}\log(1/\rho)}{\delta(1+R)}}. \tag{8.5}$$

Substituting this into the formula for the pumping velocity, (6.23), results in an explicit expression that can be differentiated to maximise U for any parameter; here, we maximise over R. Taking the derivative with respect to R and setting this to 0 results in the cubic equation

$$2\pi P_{in} R^2 \left[Q\,(R+2) + 1\right] - 8\,(R+1)^2\,(QR+1)\log(1/\rho) = 0. \tag{8.6}$$

Recall that ρ is a purely geometric parameter, independent of R. Given a Q value, this is trivially solved numerically, and the value inserted into (6.23) to compute a maximum velocity $U_{max}(Q)$. This maximum is plotted in figure 12, tracing out a black dashed line. The curve is parametrised by Q, and intersects each blue curve at its maximum value.

8.4. *Efficiency*

Now we discuss the efficiency of the pump, a concept initially defined and discussed in § 7.3. To do this, we fix the geometric parameters $\delta = 0.2$, $S = 0.1$ and $L = 0.1$, and the fluid dependent parameters R and Q. Figure 13(*a–c*) plot (all dimensionless) power input, pumping velocity per unit power and pump efficiency normalised by the electric Reynolds number, respectively, and show how each varies with the potentials $V_\perp^\pm$ (the potentials

https://doi.org/10.1017/jfm.2025.10499 Published online by Cambridge University Press

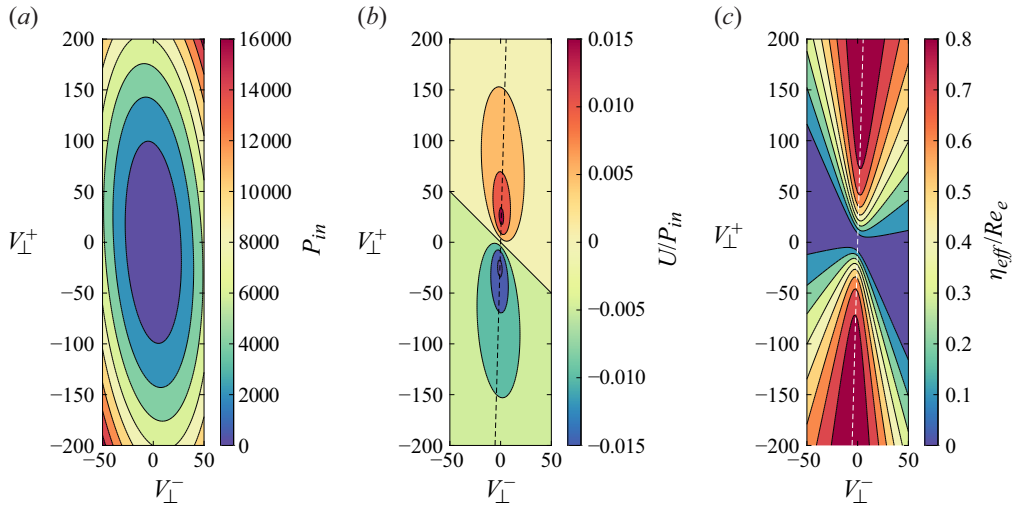


Figure 13. As functions of the upper and lower potentials (all dimensionless): (*a*) contours of power P_{in}; (*b*) contours of pumping velocity per unit power U/P_{in}; (*c*) contours of efficiency, scaled by the electric Reynolds number, η_{eff}/Re_e. In all plots, $S = L = 0.1$, $\delta = 0.2$, $Q = 1.72$ and $R = 0.027$. The values for Q and R are taken from experiments by Salipante & Vlahovska (2010), corresponding to silicone oil above and castor oil below. The two dashed lines in (*b*) and (*c*) are given by $V_\perp^+ = (1/R)V_\perp^-$, the scenario that gives the maximal pumping speed for a given P_{in}.

of the upper and lower electrodes). The equation for efficiency is given by (7.21). The values of R and Q were set at $R = 0.027$ and $Q = 1.72$, taken from droplet experiments by Salipante & Vlahovska (2010); they correspond to silicone oil as the upper fluid, and castor oil as the lower fluid. From figure 13(*a*), we see large power inputs when either $|V_\perp^+|$ or $|V_\perp^-|$ is increased, but power increases more quickly with $|V_\perp^-|$. This is because as R is small, the lower fluid is much more conductive than the upper fluid, therefore yielding significantly more current through the lower fluid when $|V_\perp^-|$ is large than in the upper fluid when $|V_\perp^+|$ is large.

Figure 13(*b*) shows that there are two global extrema for pumping velocity per unit power. In view of previous discussions, it is not surprising that the two extrema are located along the line $V_\perp^+ = (1/R)V_\perp^-$. Additionally, figure 13(*b*) shows zero velocity along $V_\perp^+ = -V_\perp^-$. Finally, figure 13(*c*) plots efficiency normalised by Re_e (assumed to be small) to create a parameter independent of the inner electrode potentials, $V_{\parallel *}$. A choice of $V_{\parallel *}$ (hence Re_e) will then simply result in a scaling of the values shown. Figure 13(*c*) shows that the pump efficiency is also generally largest along the line $V_\perp^+ = (1/R)V_\perp^-$. Interestingly, there is no global maximum, but rather the efficiency increases monotonically moving out from the origin along $V_\perp^+ = (1/R)V_\perp^-$, eventually tending towards a constant value. This happens because, by the definition of the far-field currents, the input power will scale like the potentials squared, while U increases linearly with the potentials (so the output power is also quadratic in potentials, and the efficiency is thus bounded). This linear scaling of the velocity is a consequence of our decision to scale potential fields using the inner two electrode potentials. In reality, one can expect velocities that scale linearly with both the top/bottom and inner potentials, possibly yielding quadratic growth if the far-field potentials and inner electrode potentials are scaled at the same time.

https://doi.org/10.1017/jfm.2025.10499 Published online by Cambridge University Press

9. Summary of dimensional theoretical results for optimal pumping

Finally, we summarise the closed-form theoretical results in dimensional form for the reader's convenience. The potential and velocity fields were found, assuming a small period D_* compared to height H_*, in parametric form in terms of the complex variable ζ, which lies in the annulus $\rho < |\zeta| < 1$. The upper and lower halves of the annulus correspond to the upper and lower fluids, respectively. The potential in each fluid (asymptotic composite solution) is

$$\phi_*^{\pm}(x_*, y_*) = V_{\parallel *}\left(1 \mp \frac{2}{\pi}\arg\zeta\right) + \mathrm{Re}\left[W_*^{\pm}(\zeta)\right], \tag{9.1}$$

$$W_*^{+}(\zeta) = -\frac{D_*}{\sigma^+ + \sigma^-}\left[\frac{(\sigma^-/\sigma^+)I_*^+ + I_*^-}{2\pi}\log\eta(\zeta) + \frac{I_*^+ - I_*^-}{2\pi}\log\xi(\zeta)\right],$$

$$W_*^{-}(\zeta) = -\frac{D_*}{\sigma^+ + \sigma^-}\left[\frac{I_*^+ + (\sigma^+/\sigma^-)I_*^-}{2\pi}\log\eta(\zeta) - \frac{I_*^+ - I_*^-}{2\pi}\log\xi(\zeta)\right], \tag{9.2}$$

where the complex conformal map is

$$z_* = x_* + \mathrm{i}y_* = Z_*(\zeta) = -\frac{\mathrm{i}D_*}{2\pi}\log\eta(\zeta), \tag{9.3}$$

with

$$\eta(\zeta) = M\frac{P(\zeta/\alpha,\,\rho)\,P(\zeta\alpha,\,\rho)}{P(\zeta/\overline{\alpha},\,\rho)\,P(\zeta\overline{\alpha},\,\rho)}, \quad \xi(\zeta) = \frac{P(\zeta/\alpha,\,\rho)\,P(\zeta\overline{\alpha},\,\rho)}{P(\zeta/\overline{\alpha},\,\rho)\,P(\zeta\alpha,\,\rho)}, \tag{9.4}$$

and $P(\zeta,\,\rho)$ given by (A8) (and M is such that $|\eta(\zeta)| \equiv 1$). The parameters $\alpha = \mathrm{i}r$ and ρ depend on the geometric parameters L and S, and can be determined from the solution of two simple nonlinear equations. The current densities leaving/entering the top/bottom electrodes are

$$I_*^+ = \frac{1}{H_*}\frac{((\sigma^+/\sigma^-)H^* + D_*\Lambda)\sigma^+V_{\perp *}^+ + D_*\Lambda\sigma^+V_{\perp *}^-}{(\sigma^+/\sigma^-)H_* + (\sigma^+/\sigma^- + 1)D_*\Lambda}, \tag{9.5}$$

$$I_*^- = \frac{1}{H_*}\frac{D_*\Lambda\sigma^+V_{\perp *}^+ + (1 + D_*\Lambda)\sigma^+V_{\perp *}^-}{(\sigma^+/\sigma^-)H_* + (\sigma^+/\sigma^- + 1)D_*\Lambda}, \tag{9.6}$$

where Λ is given by (4.9). The total current flowing from the high-potential ($+V_{\parallel *}$) inner electrode to the low-potential ($-V_{\parallel *}$) inner electrode is given by

$$(I_{1*} - I_{2*})/2 = V_{\parallel *}\left(\sigma^+ + \sigma^-\right)\frac{2}{\pi}\log(1/\rho)\,. \tag{9.7}$$

The pumping velocity in both fluids can in general be found using an integral derived from the reciprocal theorem, requiring integration along the fluid–fluid interfaces only. The case of maximal pumping (which is when $V_{\perp *}^+/\sigma^+ = V_{\perp *}^-/\sigma^-$) conveniently simplifies to the closed-form result

$$U_* = \frac{2\sigma^+\left(\epsilon^-/\sigma^- - \epsilon^+/\sigma^+\right)V_{\parallel *}V_{\perp *}^+}{(\mu^+ + \mu^-)(H_* + D_*\lambda_\perp)}\left(-\frac{1}{4\pi^2}\right)$$

$$\times\left(\int_{C_0^+} - \int_{C_1^+}\right)\log\left|\frac{P(\zeta/\alpha,\,\rho)\,P(\zeta\bar{\alpha},\,\rho)}{P(\zeta/\bar{\alpha},\,\rho)\,P(\zeta\alpha,\,\rho)}\right|\frac{\mathrm{d}\zeta}{\mathrm{i}\zeta}, \tag{9.8}$$

https://doi.org/10.1017/jfm.2025.10499 Published online by Cambridge University Press

where $\lambda_\perp$ is (6.11), and C_0^+ and C_0^- are the outer and inner semicircular boundaries (traversed anticlockwise) of the upper half-annulus. Moreover, the detailed analytical solution for the velocity field has been found in this optimal pumping case (not just the pumping speed). An asymptotic composite solution (valid throughout the domain of each fluid) for the streamfunction is

$$\psi_*^\pm = \mathrm{Im}\left[(\overline{z}_* - z_*)\, f_*^\pm(z_*)\right], \tag{9.9}$$

where there is reflectional symmetry, $f_*^-(z_*) = \overline{f_*^+(\overline{z_*})}$, and

$$f_*^+(Z_*(\zeta)) = \frac{H_*}{D_*}\frac{\mathrm{i}\sigma^+(\epsilon^-/\sigma^- - \epsilon^+/\sigma^+)V_{\parallel *}V_{\perp *}^+}{2(\mu^+ + \mu^-)(H_* + D_*\lambda_\perp)} \times \left[\frac{1}{2} + \sum_{n=1}^{\infty}\frac{2}{1+\rho^n}\left(\frac{1-(-1)^2}{(\pi n)^2}\right)\left(\zeta^n + \frac{\rho^n}{\zeta^n}\right)\right] - \frac{U_*}{4D_*}\mathrm{i}z_*. \tag{9.10}$$

From this, another expression for U_* arises (by considering the limit $\zeta \to \alpha = \mathrm{i}r$ in the above), given by

$$U_* = \frac{4\sigma^+(\epsilon^-/\sigma^- - \epsilon^+/\sigma^+)V_{\parallel *}V_{\perp *}^+}{\pi^2(\mu^+ + \mu^-)\,(H_* + D_*\lambda_\perp)}\sum_{m=1}^{\infty}\frac{(-1)^{m+1}}{(2m-1)^2(1+\rho^{2m-1})}\left(r^{2m-1} - \left(\frac{\rho}{r}\right)^{2m-1}\right). \tag{9.11}$$

Finally, the total power consumed per period per unit depth is given by

$$P_{in*} = D_*\left(V_{\perp *}^+ I_*^+ + V_{\perp *}^- I_*^-\right) + V_{\parallel *}\,(I_{1*} - I_{2*}). \tag{9.12}$$

9.1. *Example calculations*

To provide intuition on the ability of this pump to move leaky dielectrics, here we calculate some device metrics for realistic parameter sets. We return to the experiments of Salipante & Vlahovska (2010), who studied droplets of silicone oil in a castor oil medium. We choose silicone oil ($\epsilon^+/\epsilon_0 = 3.0$, $\sigma^+ = 1.23\times10^{-12}$ S m^{-1}, $\mu^+ = 0.97$ kg m^{-1}s^{-1}) to be the upper fluid, and castor oil ($\epsilon^-/\epsilon_0 = 5.3$, $\sigma^- = 4.5\times10^{-11}$ S m^{-1}, $\mu^- = 0.69$ kg m^{-1}s^{-1}) to be the lower fluid. The parameter $\epsilon_0 = 8.85\times10^{-12}$ F m^{-1} is the permittivity of free space. Next, we choose $D_* = 2$ mm and $H_* = 1$ cm so that $\delta = 0.2$, $S = L = 0.1$, and the smallest feature size is 200 μm. Finally, we choose $V_{\parallel *} = 0.1$ kV and $V_{\perp *}^+ = 2$ kV (this is the same as in table 1) with $V_{\perp *}^- = V_{\perp *}^+ R$. This results in $U_* \approx 0.5$ mm s^{-1}, with power consumption $P_{in*} = 2.5\times10^{-6}$ W per period per unit depth. If the microchannel is 10 cm long and 2 mm wide, then there are 50 total periods, and the pump would require a total of approximately 0.26 μW to run.

10. Discussion

In this paper, we presented a microfluidic architecture for pumping a pair of leaky-dielectric liquids in a channel, driven by Maxwell stresses on common liquid–liquid interfaces (menisci). Gradients in interfacial charge were induced with an alternating array of positive and negative electrodes inserted into the liquid–liquid interface (inducing current flow 'parallel' to the interface), and an upper and a lower electrode in the far field (inducing current flow 'normal' to the interface). The necessary existence of both normal and tangential electric field gradients leads to Maxwell stresses on the fluids, and due to asymmetric spacing of the interfacial electrodes, a net flow.

https://doi.org/10.1017/jfm.2025.10499 Published online by Cambridge University Press

To explore the theoretical potential of such a design, we assumed the Taylor–Melcher leaky-dielectric model and Stokes flow, and proceeded to solve for the electric potential and resulting pumping speeds. To make analytical progress, we neglected charge advection (zero electric Reynolds number), and considered the geometric limit where the inner electrode period is small in comparison to the channel thickness (i.e. distance between the far-field electrodes). This enabled the use of matched asymptotic expansions, whereby the liquid domains decomposed into an 'inner region' close to the liquid interfaces, and 'outer regions' above and below where the fields appear one-dimensional (up to exponentially small errors). The electrical problem in the inner region was then a non-trivial two-phase one, which was exactly solvable using complex variable techniques. It was a superposition of two current flow problems: (i) current flow between the inner electrodes (solution following from prior work); (ii) current flow to/from the far field, with the inner electrodes grounded. This latter solution, presented in § 4 (and derived in Appendix A) will likely have applications to other physical two-phase problems governed by Laplace's equation. Our analysis yielded an explicit formula for the pumping speed for any choice of electrode potentials. Moreover, the entire flow fields for both liquids were found to be identical, up to reflection in their contact plane, no matter their viscosities. During our analysis, we also assumed that the menisci were flat (small capillary number), which facilitated the analytical methods used, but this could be relaxed by the use of boundary perturbations or different complex methods. Similar flows over periodic surfaces with curved menisci have been solved with analytical methods in the context of superhydrophobic surfaces (Crowdy 2016, 2017), and could potentially be employed here.

Next, we investigated the optimal choice of control parameters, in particular the electrode potentials, that maximise pumping velocity. We found that by varying the electrode potentials relative to each other, one has control over the magnitude and direction (i.e. to the left or right) of the pumping. For a given input power, the magnitude is limited by a maximum value that depends on the liquid conductivity and permittivity ratios (R and Q), and the inner electrode spacing/width. This maximum occurs when there is net-zero current flowing from the inner electrodes, i.e. when the component of the current flowing to/from the far field is uniform (or unidirectional) – this is easily ensured by choosing the electrode potentials appropriately. This 'optimal pumping' scenario has even simpler formulas, and we conveniently provide the entire (composite) velocity field in closed form. This optimal pumping speed can be achieved in either direction, given a liquid pair and geometry, by simply exchanging (up to a factor of R) the potentials of the far-field electrodes. In general, the pumping direction depends on the sign of $RQ - 1$, the electrode potentials, and also the spacing of the inner electrodes, thus it has several control pathways. For example, the set of positive and negative inner electrodes can be realised practically using two interdigitated combs, hence these could be moved relative to each other mechanically, changing the electrode spacing and hence flow direction.

Pumping efficiency – the ratio of mechanical output power to electrical input power – was also analysed, and found to be maximised by maximising pumping velocity, which is perhaps expected. However, the efficiency increases towards a maximum as the magnitude of the far-field potentials is increased (relative to the inner electrodes). The efficiency is, however, proportional to the electric Reynolds number ($\eta_{eff} = O(Re_e)$), which we assumed here to be small for tractability, thus the efficiencies are not expected to be significant. If greater efficiency is desired, then one could consider scenarios with larger Re_e values, and this would necessitate the inclusion of charge advection on the interfaces.

Employing periodic, asymmetric structures, as we have done here, has many general advantages for microfluidic pumping, as pointed out by Ajdari (2000). A major advantage

https://doi.org/10.1017/jfm.2025.10499 Published online by Cambridge University Press

is that no global (or macroscale) electric potential gradients in the direction of flow are necessary; only local (or microscale) potential gradients are employed, with the global net flow arising from symmetry breaking. This is particularly significant for leaky-dielectric fluids, which, due to their very low conductivity, would need prohibitively large streamwise potential drops in a simple planar channel geometry, thus pumping would be limited to short channels. However, the periodic design considered here has no limit on the length of the channel.

In order to employ Maxwell stresses here for fluid pumping, it was necessary to induce a surface charge on the liquid–liquid interfaces, and we achieved that here by imposing a normal electric field with additional upper and lower electrodes. This may not be ideal, given that this implies an additional flow of current and therefore energy losses, so exploring other set-ups to generate normal electric fields in future work may be advantageous, e.g. altering the shape of the inner electrodes in an asymmetric fashion.

Finally, although we have focused on the combination of silicone oil and castor oil, there are many other fluids that could be pumped with this architecture, including the mineral oils and fluorinated oils often used in microfluidic droplet generation (Moragues *et al.* 2023). In fact, a whole class of fluids, so-called electroconjugate fluids, are leaky dielectrics that have been used to generate jet-like flows using breaks in symmetry of normal Maxwell stresses (Raghavan *et al.* 2009). Additionally, beyond leaky dielectrics, our mathematical model loses its efficacy but the geometry presented here should still provide pumping power. As an example, Pascall & Squires (2011) considered the electrokinetic behaviour of electrolyte–electrolyte interfaces and electrolyte–liquid metal interfaces. If, say, you considered such fluid combinations in our geometry, then the break in symmetry of our electrodes may still cause significant electrokinetic flow. Set up in this manner, the device could be viewed as the fluid–fluid counterpart to the Ajdari initial pump design (Ajdari 2000). This is a possible source of future modelling work that could lead to significant microfluidic pumping.

Funding. M.D.M. and D.G.C. are supported by CBET-EPSRC grant EP/V062298/1. T.L.K. was supported by a Chapman Fellowship in the Department of Mathematics, Imperial College London.

Declaration of interests. The authors report no conflict of interest.

Appendix A. Derivation of far-field current flow past interfacial electrodes

This appendix focuses on the derivation of the unbounded two-phase problem, where the far-field currents in both phases are in general different, and the interfacial electrodes are grounded. This appears as one component of the inner solution, close to the interface $y = 0$, embedded within a finite channel as described in § 3.

It is necessary to determine the two fields $\Phi^{\pm}(X, Y)$, which are harmonic in the upper ($Y > 0$) and lower ($Y < 0$) semi-strips, respectively, as shown in figure 14. They satisfy conditions (3.32)–(3.34) on the interface $Y = 0$, with far-field behaviours

$$\Phi^{+} \sim I^{+}Y, \quad Y \to +\infty, \tag{A1}$$

$$\Phi^{-} \sim RI^{-}Y, \quad Y \to -\infty. \tag{A2}$$

A.1. *The complex potentials*

Let

$$w^{+}(z) = \Phi^{+} + \mathrm{i}\chi^{+}, \quad w^{-}(z) = \Phi^{-} + \mathrm{i}\chi^{-}, \quad \text{where } z = X + \mathrm{i}Y, \tag{A3}$$

https://doi.org/10.1017/jfm.2025.10499 Published online by Cambridge University Press

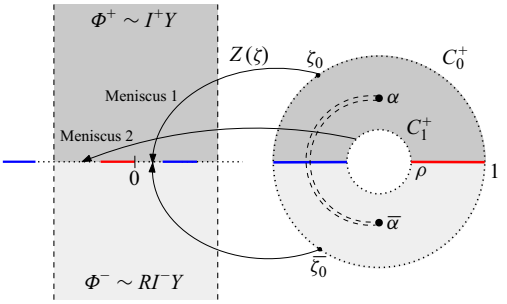


Figure 14. Two-phase electric field problem on either side of a grating of electrodes. There are two electrodes per period. The period is taken to be unity. The upper half-annulus maps to the upper-half period strip, and the lower half-annulus maps to the lower-half period strip. An important fact is that if the mapping $Z(\zeta)$ in (A7) takes ζ_0 on C_0^+ to a point z_0 on meniscus 1, then it transplants the complex conjugate point $\overline{\zeta_0}$ on C_0^- to the same point.

denote the complex potentials in the upper (+) and lower (−) period semi-strips, assumed to be of unit period. The boundary conditions (A1)–(A2) necessitate that

$$\begin{aligned} w^+(z) &\sim -\mathrm{i}I^+ z \quad \text{as } Y \to +\infty, \\ w^-(z) &\sim -\mathrm{i}RI^- z \quad \text{as } Y \to -\infty. \end{aligned} \tag{A4}$$

The electrodes are grounded, (3.32), and the continuity conditions on the menisci, (3.33)–(3.34), can be written using the Cauchy–Riemann relations as

$$\Phi^+ = \Phi^-, \quad \frac{\partial \chi^+}{\partial X} = \frac{1}{R}\frac{\partial \chi^-}{\partial X}. \tag{A5}$$

On integration of the second condition along the menisci, it can be inferred that

$$\Phi^+ = \Phi^-, \quad \chi^+ = \begin{cases} \chi^-/R + c_1 & \text{on meniscus 1}, \\ \chi^-/R + c_2 & \text{on meniscus 2}, \end{cases} \tag{A6}$$

where c_1 and c_2 are real-valued constants. Without loss of generality, one of these can be set to zero (but not both).

A.2. *Conformal mapping*

The conformal mapping function

$$z = Z(\zeta) = -\frac{\mathrm{i}}{2\pi}\log \eta(\zeta), \tag{A7}$$

where

$$\eta(\zeta) = M\frac{P(\zeta/\alpha,\, \rho)\; P(\zeta\alpha,\, \rho)}{P(\zeta/\overline{\alpha},\, \rho)\; P(\zeta\overline{\alpha},\, \rho)}, \quad P(\zeta,\, \rho) = (1-\zeta)\prod_{n=1}^{\infty}(1-\rho^{2n}\zeta)(1-\rho^{2n}/\zeta), \tag{A8}$$

with $\alpha = \mathrm{i}r$ for $\rho < r < 1$, transplants the upper half-annulus

$$\rho < |\zeta| < 1, \quad \mathrm{Im}[\zeta] \geqslant 0, \tag{A9}$$

to the upper-half period strip – see figure 14. This mapping is familiar from Crowdy (2011) and Crowdy *et al.* (2023) (see also Crowdy 2020). The two real-axis portions $\rho < \zeta < 1$ and $-1 < \zeta < -\rho$ are transplanted to the two grounded electrodes of equal length; the

https://doi.org/10.1017/jfm.2025.10499 Published online by Cambridge University Press

upper half-circle

$$C_0^+ = \{\zeta \,:\, |\zeta| = 1,\ \mathrm{Im}[\zeta] \geqslant 0\} \tag{A10}$$

is transplanted to meniscus 1, and the upper half-circle

$$C_1^+ = \{\zeta \,:\, |\zeta| = \rho,\ \mathrm{Im}[\zeta] \geqslant 0\} \tag{A11}$$

is transplanted to meniscus 2. The constant M is taken to be

$$M = \frac{P(1/\overline{\alpha},\, \rho)\ P(\overline{\alpha},\, \rho)}{P(1/\alpha,\, \rho)\ P(\alpha,\, \rho)}, \tag{A12}$$

to ensure that the section of the annulus on the positive real axis maps to the electrode plate pinned to (the left of) the origin in figure 14, i.e. $Z(1) = 0$. The constants ρ and $\alpha = \mathrm{i}r$ are fixed by the requirements that

$$Z(\rho) = -L, \quad Z(-1) = S, \tag{A13}$$

furnishing two algebraic equations for the two unknown ρ and r. It is the fact that α is chosen on the imaginary axis that means that the two electrodes are of equal length. A generalisation to unequal electrodes simply requires α to be a more general point in the upper half-annulus $\rho < |\zeta| < 1,\ \mathrm{Im}[\zeta] > 0$. It turns out that the same mapping transplants the lower half-annulus

$$\rho < |\zeta| < 1, \quad \mathrm{Im}[\zeta] \leqslant 0, \tag{A14}$$

to the lower half-period strip.

The function $P(\zeta, \rho)$, which is closely related to the so-called prime function of the annulus (Crowdy 2020), satisfies two important functional relations:

$$P(\zeta^{-1}, \rho) = -\zeta^{-1}\, P(\zeta, \rho), \quad P(\rho^2\zeta, \rho) = -\zeta^{-1}\, P(\zeta, \rho). \tag{A15}$$

These can be verified from the infinite product definition (A8). An important observation is that if z is a point on either meniscus with pre-image ζ on either C_0^+ or C_1^+, then the image of $\overline{\zeta}$, which lies on the boundary of the lower half-annulus, is the same point z.

A.3. *Solution method*

Define the two composed functions

$$W^+(\zeta) \equiv w^+(Z(\zeta)), \quad W^-(\zeta) \equiv w^-(Z(\zeta)). \tag{A16}$$

First note that by (3.32),

$$\mathrm{Re}[W^+(\zeta)] = \mathrm{Re}[W^-(\zeta)] = 0 \quad \text{on } \overline{\zeta} = \zeta. \tag{A17}$$

This implies that the Schwarz conjugate functions $\overline{W_\pm}(\zeta)$ defined by

$$\overline{W^\pm}(\zeta) = \overline{W^\pm(\overline{\zeta})} \tag{A18}$$

satisfy the functional relations

$$\overline{W^\pm}(\zeta) = -W^\pm(\zeta). \tag{A19}$$

It is important to study the singularity structure of $W^\pm(\zeta)$ inside the annulus $\rho < |\zeta| < 1$. Since, as $\zeta \to \alpha$,

$$Z(\zeta) \sim -\frac{\mathrm{i}}{2\pi}\log(\zeta - \alpha), \tag{A20}$$

https://doi.org/10.1017/jfm.2025.10499 Published online by Cambridge University Press

we have, by (A4), as $\zeta \to \alpha$,

$$W^+(\zeta) \sim -\frac{I^+}{2\pi} \log(\zeta - \alpha). \tag{A21}$$

By (A19), it can be inferred, by a Schwarz reflection argument, that

$$W^+(\zeta) = -\frac{I^+}{2\pi} \log\left(\frac{\zeta - \alpha}{\zeta - \overline{\alpha}}\right) + \text{a function analytic in the annulus.} \tag{A22}$$

Similar arguments reveal that

$$W^-(\zeta) = -\frac{RI^-}{2\pi} \log\left(\frac{\zeta - \alpha}{\zeta - \overline{\alpha}}\right) + \text{a function analytic in the annulus.} \tag{A23}$$

The condition (A6) on meniscus 1 implies that on C_0,

$$\mathrm{Re}[W^+(\zeta)] = \mathrm{Re}[W^-(\overline{\zeta})], \qquad \mathrm{Im}[W^+(\zeta)] = \frac{1}{R}\,\mathrm{Im}[W^-(\overline{\zeta})] + c_1, \tag{A24}$$

where use has been made of the fact that complex conjugate points on C_0 correspond to the same point on the meniscus. The first of these implies that

$$W^+(\zeta) + \overline{W^+}(\overline{\zeta}) = W^-(\overline{\zeta}) + \overline{W^-}(\zeta). \tag{A25}$$

This can be written

$$W^+(\zeta) + \overline{W^+}(1/\zeta) = W^-(1/\zeta) + \overline{W^-}(\zeta) \tag{A26}$$

or, on rearrangement,

$$W^+(\zeta) - \overline{W^-}(\zeta) = -(\overline{W^+}(1/\zeta) - W^-(1/\zeta)). \tag{A27}$$

Using (A19), this becomes

$$W^+(\zeta) + W^-(\zeta) = -(\overline{W^+}(1/\zeta) + \overline{W^-}(1/\zeta)). \tag{A28}$$

This can be restated as

$$\mathrm{Re}[F(\zeta)] = 0 \quad \text{on } C_0, \tag{A29}$$

with

$$F(\zeta) \equiv W^+(\zeta) + W^-(\zeta). \tag{A30}$$

The second condition in (A24) implies that

$$W^+(\zeta) - \overline{W^+}(\overline{\zeta}) = \frac{1}{R}(W^-(\overline{\zeta}) - \overline{W^-}(\zeta)) + 2\mathrm{i}c_1, \tag{A31}$$

or

$$W^+(\zeta) - \overline{W^+}(1/\zeta) = \frac{1}{R}(W^-(1/\zeta) - \overline{W^-}(\zeta)) + 2\mathrm{i}c_1. \tag{A32}$$

On rearrangement,

$$W^+(\zeta) + \frac{1}{R}\overline{W^-}(\zeta) = \overline{W^+}(1/\zeta) + \frac{1}{R}W^-(1/\zeta) + 2\mathrm{i}c_1. \tag{A33}$$

Using (A19), this becomes

$$W^+(\zeta) - \frac{1}{R}W^-(\zeta) = \overline{W^+}(1/\zeta) - \frac{1}{R}\overline{W^-}(1/\zeta) + 2\mathrm{i}c_1. \tag{A34}$$

https://doi.org/10.1017/jfm.2025.10499 Published online by Cambridge University Press

This can be restated as

$$\mathrm{Im}[G(\zeta)] = c_1 \quad \text{on } C_0, \tag{A35}$$

with

$$G(\zeta) \equiv W^+(\zeta) - \frac{1}{R} W^-(\zeta). \tag{A36}$$

An identical set of arguments on the other meniscus, corresponding to C_1, can be used to show that

$$\mathrm{Re}[F(\zeta)] = 0 \quad \text{on } C_1, \tag{A37}$$

$$\mathrm{Im}[G(\zeta)] = c_2 \quad \text{on } C_1. \tag{A38}$$

From (A22) and (A23), it can be deduced that inside the annulus $\rho < |\zeta| < 1$,

$$F(\zeta) = -\frac{I^+ + RI^-}{2\pi} \log\left(\frac{\zeta - \alpha}{\zeta - \overline{\alpha}}\right) + \text{a function analytic in the annulus} \tag{A39}$$

and

$$G(\zeta) = -\frac{I^+ - I^-}{2\pi} \log\left(\frac{\zeta - \alpha}{\zeta - \overline{\alpha}}\right) + \text{a function analytic in the annulus.} \tag{A40}$$

If $F(\zeta)$ and $G(\zeta)$ can be found, then from their definitions (A30) and (A36), it follows that

$$W^+(\zeta) = \frac{1}{R+1}(F(\zeta) + RG(\zeta)), \quad W^-(\zeta) = \frac{R}{R+1}(F(\zeta) - G(\zeta)). \tag{A41}$$

It is now posed, based on conformal slit mapping ideas presented elsewhere (Crowdy 2011, 2012, 2020), that admissible $F(\zeta)$ and $G(\zeta)$ are given by

$$F(\zeta) = -\mathrm{i}(I^+ + RI^-)\, Z(\zeta), \quad G(\zeta) = -\frac{I^+ - I^-}{2\pi} \log \xi(\zeta), \tag{A42}$$

where

$$\xi(\zeta) = \frac{P(\zeta/\alpha,\, \rho)\, P(\zeta\overline{\alpha},\, \rho)}{P(\zeta/\overline{\alpha},\, \rho)\, P(\zeta\alpha,\, \rho)}. \tag{A43}$$

This choice corresponds to $c_2 = 0$. First, note that

$$\overline{F}(\zeta) = \mathrm{i}(I^+ + RI^-)\overline{Z}(\zeta) = -F(\zeta), \tag{A44}$$

and that

$$\overline{G}(\zeta) = -\frac{I^+ - I^-}{2\pi} \log \overline{\xi}(\zeta) = -\frac{I^+ - I^-}{2\pi} \log(1/\xi(\zeta)) = -G(\zeta), \tag{A45}$$

thus confirming that both functions given in (A41) satisfy (A19), as required. It is also clear from the given functional forms that $F(\zeta)$ and $G(\zeta)$ have the singularity structure given in (A39) and (A40).

It is easy to check, using the properties of the mapping function $Z(\zeta)$ and the properties (A15), that $F(\zeta)$ satisfies condition (A29) on C_0, and condition (A37) on C_1. To confirm that $G(\zeta)$ satisfies (A35) on C_0, and condition (A38) on C_1, it is noted that, as shown in Chapter 5 of Crowdy (2020), the function $\xi(\zeta)$ is a radial slit mapping from the annulus $\rho < |\zeta| < 1$ that takes C_0 and C_1 to radial slits, with the two real axis portions $-1 < \zeta < -\rho$ and $\rho < \zeta < 1$ being transplanted to the unit circle, i.e. $|\xi(\zeta)| = 1$ for $-1 < \zeta < -\rho$ and $\rho < \zeta < 1$. In particular, the fact that C_0 and C_1 are transplanted by

https://doi.org/10.1017/jfm.2025.10499 Published online by Cambridge University Press

$\xi(\zeta)$ to radial slits, where $\xi(\zeta)$ has constant argument, means that $G(\zeta)$ satisfies (A35) on C_0, and condition (A38) on C_1.

On substitution of the functional forms (A42) into (A41), we arrive at the final results:

$$W^+(\zeta) = -\frac{R}{R+1}\left[\frac{I^+ + RI^-}{2\pi R}\log\eta(\zeta) + \frac{I^+ - I^-}{2\pi}\log\xi(\zeta)\right],$$
$$W^-(\zeta) = -\frac{R}{R+1}\left[\frac{I^+ + RI^-}{2\pi}\log\eta(\zeta) - \frac{I^+ - I^-}{2\pi}\log\xi(\zeta)\right]. \tag{A46}$$

The required potentials $\Phi^\pm$ then follow as the real parts of the two functions in (A46). The relevant value of c_1 can be found from this solution (note that we chose $c_2 = 0$), and it turns out to correspond to the total current flowing out of a single interfacial electrode. This is easily computed by a global current balance to be $c_1 = (I^- - I^+)/2$.

Any pure imaginary constant can be added to this solution pair, and this will not affect the grounded condition on the electrodes or the continuity conditions across the menisci.

A.4. *Special case: $I^- = I^+$*

When $I^- = I^+$, (A46) reduces to

$$W^+(\zeta) = -\frac{1}{R+1}\left[\frac{I^+ + RI^-}{2\pi}\log\eta(\zeta)\right] = -\frac{I^+}{2\pi}\log\eta(\zeta),$$
$$W^-(\zeta) = -\frac{R}{R+1}\left[\frac{I^+ + RI^-}{2\pi}\log\eta(\zeta)\right] = -\frac{RI^+}{2\pi}\log\eta(\zeta), \tag{A47}$$

which correspond to the trivial solutions

$$w^+(z) = -\mathrm{i}I^+ z, \quad w^-(z) = -\mathrm{i}RI^- z. \tag{A48}$$

A.5. *Special case: $R = 1$*

When $R = 1$, which is the case of a single fluid occupying both regions, it can be verified that all potential fields are continuous on the menisci. These checks are performed in Appendix B.

A.6. *Far-field behaviours*

A useful observation following from (A8) and (A43) (and used previously in Crowdy 2011) is that

$$\xi(\zeta) = \frac{\eta(\zeta)}{M}\left(\frac{P(\zeta\overline{\alpha}, \rho)}{P(\zeta\alpha, \rho)}\right)^2. \tag{A49}$$

Therefore, (A46) can be written as

$$W^+(\zeta) = -\mathrm{i}I^+ Z(\zeta) + \frac{R(I^+ - I^-)}{2\pi(R+1)}\log\left[M\left(\frac{P(\zeta\alpha, \rho)}{P(\zeta\overline{\alpha}, \rho)}\right)^2\right],$$
$$W^-(\zeta) = -\mathrm{i}RI^- Z(\zeta) - \frac{R(I^+ - I^-)}{2\pi(R+1)}\log\left[M\left(\frac{P(\zeta\alpha, \rho)}{P(\zeta\overline{\alpha}, \rho)}\right)^2\right]. \tag{A50}$$

Since $\zeta \to \alpha$ corresponds to $Y \to +\infty$, it can be inferred that

$$w^+(z) \sim -\mathrm{i}I^+ z + \lambda^+, \tag{A51}$$

https://doi.org/10.1017/jfm.2025.10499 Published online by Cambridge University Press

where

$$\lambda^+ = \frac{R(I^+ - I^-)}{2\pi(R+1)} \log\left[M \left(\frac{P(\alpha^2, \rho)}{P(|\alpha|^2, \rho)} \right)^2 \right]. \tag{A52}$$

Similarly, since $\zeta \to \overline{\alpha}$ corresponds to $Y \to -\infty$, we have

$$w^-(z) \sim -\mathrm{i}RI^- z + \lambda^-, \tag{A53}$$

where

$$\lambda^- = -\frac{R(I^+ - I^-)}{2\pi(R+1)} \log\left[M \left(\frac{P(|\alpha|^2, \rho)}{P(\overline{\alpha}^2, \rho)} \right)^2 \right]. \tag{A54}$$

On taking the real part, it follows that (using $|M| = 1$)

$$\Phi^+ \sim I^+ Y + (I^+ - I^-)\Lambda, \quad \Phi^- \sim RI^- Y + (I^+ - I^-)\Lambda, \tag{A55}$$

where

$$\Lambda = \frac{R}{\pi(R+1)} \log\left| \frac{P(\alpha^2, \rho)}{P(|\alpha|^2, \rho)} \right|. \tag{A56}$$

It is worth pointing out that this formula is reminiscent of that derived in Crowdy (2011) for an 'effective slip length' relevant in the problem considered there.

Appendix B. Solution for far-field current flow: special case $R = 1$

In this appendix, we consider the complex variable solution in the inner region for far-field current flow (and grounded interfacial electrodes) in the special case $R = 1$, i.e. the conductivities of the two fluids are the same. This corresponds to the case of a single fluid occupying both regions, and here we verify that the complex potentials are continuous on the menisci. This is more subtle than it appears: it must be verified, for meniscus 1, that when $\zeta \in C_0$,

$$W^+(\zeta) = W^-(\overline{\zeta}), \tag{B1}$$

and not that $W^+(\zeta) = W^-(\zeta)$. Note, however, that

$$\eta(1/\zeta) = M \frac{P(1/(\zeta\alpha), \rho)\, P(\alpha/\zeta, \rho)}{P(1/(\zeta\overline{\alpha}), \rho)\, P(\overline{\alpha}/\zeta, \rho)} = M \frac{P(\zeta\alpha, \rho)\, P(\zeta/\alpha, \rho)}{P(\zeta\overline{\alpha}, \rho)\, P(\zeta/\overline{\alpha}, \rho)} = \eta(\zeta) \tag{B2}$$

but that

$$\xi(1/\zeta) = \frac{P(1/(\zeta\alpha), \rho)\, P(\overline{\alpha}/\zeta, \rho)}{P(1/(\zeta\overline{\alpha}), \rho)\, P(\alpha/\zeta, \rho)} = \frac{P(\zeta\alpha, \rho)\, P(\zeta/\overline{\alpha}, \rho)}{P(\zeta\overline{\alpha}, \rho)\, P(\zeta/\alpha, \rho)} = \frac{1}{\xi(\zeta)}. \tag{B3}$$

When $R = 1$,

$$\begin{aligned} W^+(\zeta) &= -\frac{1}{2}\left[\frac{I^+ + I^-}{2\pi} \log \eta(\zeta) + \frac{I^+ - I^-}{2\pi} \log \xi(\zeta) \right], \\ W^-(\zeta) &= -\frac{1}{2}\left[\frac{I^+ + I^-}{2\pi} \log \eta(\zeta) - \frac{I^+ - I^-}{2\pi} \log \xi(\zeta) \right], \end{aligned} \tag{B4}$$

https://doi.org/10.1017/jfm.2025.10499 Published online by Cambridge University Press

therefore on C_0 where $\overline{\zeta} = 1/\zeta$,

$$\begin{aligned} W^+(\zeta) &= -\frac{1}{2}\left[\frac{I^+ + I^-}{2\pi}\log\eta(\zeta) + \frac{I^+ - I^-}{2\pi}\log\xi(\zeta)\right], \\ W^-(1/\zeta) &= -\frac{1}{2}\left[\frac{I^+ + I^-}{2\pi}\log\eta(1/\zeta) - \frac{I^+ - I^-}{2\pi}\log\xi(1/\zeta)\right] \\ &= -\frac{1}{2}\left[\frac{I^+ + I^-}{2\pi}\log\eta(\zeta) + \frac{I^+ - I^-}{2\pi}\log\xi(\zeta)\right], \end{aligned} \tag{B5}$$

thereby confirming (B1).

On meniscus 2, on the other hand, it must be checked that for $\zeta \in C_1$,

$$W^+(\zeta) = W^-(\overline{\zeta}) = W^-(\rho^2/\zeta). \tag{B6}$$

Note, however, that

$$\eta(\rho^2/\zeta) = \frac{P(\rho^2/(\zeta\alpha),\rho)\,P(\rho^2\alpha/\zeta,\rho)}{P(\rho^2/(\zeta\overline{\alpha}),\rho)\,P(\rho^2\overline{\alpha}/\zeta,\rho)} = \frac{P(\zeta\alpha,\rho)\,P(\zeta/\alpha,\rho)}{P(\zeta\overline{\alpha},\rho)\,P(\zeta/\overline{\alpha},\rho)} = \eta(\zeta), \tag{B7}$$

but that

$$\xi(\rho^2/\zeta) = \frac{P(\rho^2/(\zeta\alpha),\rho)\,P(\rho^2\overline{\alpha}/\zeta,\rho)}{P(\rho^2/(\zeta\overline{\alpha}),\rho)\,P(\rho^2\alpha/\zeta,\rho)} = \frac{P(\zeta\alpha,\rho)\,P(\zeta/\overline{\alpha},\rho)}{P(\zeta\overline{\alpha},\rho)\,P(\zeta/\alpha,\rho)} = \frac{1}{\xi(\zeta)}. \tag{B8}$$

Therefore, from (B4), on C_1 where $\overline{\zeta} = \rho^2/\zeta$,

$$\begin{aligned} W^+(\zeta) &= -\frac{1}{2}\left[\frac{I^+ + I^-}{2\pi}\log\eta(\zeta) + \frac{I^+ - I^-}{2\pi}\log\xi(\zeta)\right], \\ W^-(\rho^2/\zeta) &= -\frac{1}{2}\left[\frac{I^+ + I^-}{2\pi}\log\eta(\rho^2/\zeta) - \frac{I^+ - I^-}{2\pi}\log\xi(\rho^2/\zeta)\right] \\ &= -\frac{1}{2}\left[\frac{I^+ + I^-}{2\pi}\log\eta(\zeta) + \frac{I^+ - I^-}{2\pi}\log\xi(\zeta)\right], \end{aligned} \tag{B9}$$

thereby confirming (B6).

References

Ajdari, A. 2000 Pumping liquids using asymmetric electrode arrays. *Phys. Rev. E* **61** (1), R45–R48.

Baygents, J.C. & Saville, D.A. 1990 The circulation produced in a drop by an electric field: a high field strength electrokinetic model. *AIP Conf. Proc.* **197** (1), 7–17.

Bazant, M.Z. 2015 Electrokinetics meets electrohydrodynamics. *J. Fluid Mech.* **782**, 1–4.

Bazant, M.Z. & Squires, T.M. 2010 Induced-charge electrokinetic phenomena. *Curr. Opin. Colloid Interface Sci.* **15** (3), 203–213.

Belousov, K.I., Filatov, N.A., Kukhtevich, I.V., Kantsler, V., Evstrapov, A.A. & Bukatin, A.S. 2021 An asymmetric flow-focusing droplet generator promotes rapid mixing of reagents. *Sci. Rep. UK* **11**, 8797.

Brown, A.B.D., Smith, C.G. & Rennie, A.R. 2001 Pumping of water with AC electric fields applied to asymmetric pairs of microelectrodes. *Phys. Rev. E* **63** (1), 1–8.

Crowdy, D.G. 2011 Frictional slip lengths for unidirectional superhydrophobic grooved surfaces. *Phys. Fluids* **23** (7), 072001.

Crowdy, D.G. 2012 Conformal slit maps in applied mathematics. *ANZIAM J.* **53** (3), 171–189.

Crowdy, D.G. 2016 Analytical formulae for longitudinal slip lengths over unidirectional superhydrophobic surfaces with curved menisci. *J. Fluid Mech.* **791**, R7.

Crowdy, D.G. 2017 Slip length for transverse shear flow over a periodic array of weakly curved menisci. *Phys. Fluids* **29**, 091702.

Crowdy, D.G. 2020 *Solving Problems in Multiply Connected Domains*. Society for Industrial and Applied Mathematics.

https://doi.org/10.1017/jfm.2025.10499 Published online by Cambridge University Press

CROWDY, D.G., MAYER, M.D. & HODES, M. 2023 Asymmetric thermocapillarity-based pump: concept and exactly solved model. *Phys. Rev. Fluids* **8** (9), 1–22.
DAS, D. & SAINTILLAN, D. 2017 Electrohydrodynamics of viscous drops in strong electric fields: numerical simulations. *J. Fluid Mech.* **829**, 127–152.
FENG, J.Q. 1999 Electrohydrodynamic behaviour of a drop subjected to a steady uniform electric field at finite electric Reynolds number. *Proc. R. Soc. Lond. A* **455**, 2245–2269.
FENG, J.Q. 2002 A 2D electrohydrodynamic model for electrorotation of fluid drops. *J. Colloid Interface Sci.* **246** (1), 112–121.
FRUMKIN, A. 1946 New electrocapillary phenomena. *J. Colloid Sci.* **1** (3), 277–291.
HE, H., SALIPANTE, P.F. & VLAHOVSKA, P.M. 2013 Electrorotation of a viscous droplet in a uniform direct current electric field. *Phys. Fluids* **25**, 3.
HODES, M., KANE, D., BAZANT, M.Z. & KIRK, T.L. 2023 Asymptotic Nusselt numbers for internal flow in the Cassie state. *J. Fluid Mech.* **977**, A18.
LANAUZE, J.A., WALKER, L.M. & KHAIR, A.S. 2015 Nonlinear electrohydrodynamics of slightly deformed oblate drops. *J. Fluid Mech.* **774**, 245–266.
LASER, D.J. & SANTIAGO, J.G. 2004 A review of micropumps. *J. Micromech. Microeng.* **14** (6), R35.
LEVICH, V.G. 1962 *Physicochemical Hydrodynamics*, 2nd edn. Prentice-Hall.
LÓPEZ-HERRERA, J.M., HERRADA, M.A. & GAÑÁN-CALVO, A.M. 2023 Electrokinetic modelling of cone-jet electrosprays. *J. Fluid Mech.* **964**, A19.
MANSURIPUR, T.S., PASCALL, A.J. & SQUIRES, T.M. 2009 Asymmetric flows over symmetric surfaces: capacitive coupling in induced-charge electro-osmosis. *New J. Phys.* **11**, 075030.
MELCHER, J.R. & TAYLOR, G.I. 1969 Electrohydrodynamics: a review of the role of interfacial shear stresses. *Annu. Rev. Fluid Mech.* **1** (1), 111–146.
MORAGUES, T., ARGUIJO, D., BENEYTON, T., MODAVI, C., SIMUTIS, K., ABATE, A.R., BARET, J.C., DEMELLO, A.J., DENSMORE, D. & GRIFFITHS, A.D. 2023 Droplet-based microfluidics. *Nat. Rev. Meth. Primers* **3**, 32.
MORI, Y. & YOUNG, Y.N. 2018 From electrodiffusion theory to the electrohydrodynamics of leaky dielectrics through the weak electrolyte limit. *J. Fluid Mech.* **855**, 67–130.
PASCALL, A.J. & SQUIRES, T.M. 2011 Electrokinetics at liquid/liquid interfaces. *J. Fluid Mech.* **684**, 163–191.
RAGHAVAN, R.V., QIN, J., YEO, L.Y., FRIEND, J.R., TAKEMURA, K., YOKOTA, S. & EDAMURA, K. 2009 Electrokinetic actuation of low conductivity dielectric liquids. *Sensors Actuators B: Chem.* **140**, 287–294.
SALIPANTE, P.F. & VLAHOVSKA, P.M. 2010 Electrohydrodynamics of drops in strong uniform DC electric fields. *Phys. Fluids* **22** (11), 112110.
SAVILLE, D.A. 1997 Electrohydrodynamics: the Taylor–Melcher leaky dielectric model. *Annu. Rev. Fluid Mech.* **29**, 27–64.
SCHNITZER, O., FRANKEL, I. & YARIV, E. 2013 Deformation of leaky-dielectric fluid globules under strong electric fields: boundary layers and jets at large Reynolds numbers. *J. Fluid Mech.* **734**, 1–12.
SCHNITZER, O. & YARIV, E. 2015 The Taylor–Melcher leaky dielectric model as a macroscale electrokinetic description. *J. Fluid Mech.* **773**, 1–33.
SHERWOOD, J.D. 1988 Breakup of fluid droplets in electric and magnetic fields. *J. Fluid Mech.* **188**, 133–146.
SQUIRES, T.M. & BAZANT, M.Z. 2004 Induced-charge electro-osmosis. *J. Fluid Mech.* **509**, 217–252.
SQUIRES, T.M. & BAZANT, M.Z. 2006 Breaking symmetries in induced-charge electro-osmosis and electrophoresis. *J. Fluid Mech.* **560**, 65–101.
STONE, H.A., STROOCK, A.D. & AJDARI, A. 2004 Engineering flows in small devices: microfluidics toward a lab-on-a-chip. *Annu. Rev. Fluid Mech.* **36**, 381–411.
TAYLOR, G.I. 1966 Studies in electrohydrodynamics. I. The circulation produced in a drop by an electric field. *Proc. R. Soc. Lond. A* **291** (1425), 159–166.
VIZIKA, O. & SAVILLE, D.A. 1992 The electrohydrodynamic deformation of drops suspended in liquids in steady and oscillatory electric fields. *J. Fluid Mech.* **239** (1), 1–21.
WANG, C. & GUO, Z. 2020 A comparison between superhydrophobic surfaces (SHS) and slippery liquid-infused porous surfaces (SLIPS) in application. *Nanoscale* **12**, 22398–22424.
ZHOLKOVSKIJ, E.K., MASLIYAH, J.H. & CZARNECKI, J. 2002 An electrokinetic model of drop deformation in an electric field. *J. Fluid Mech.* **472**, 1–27.

https://doi.org/10.1017/jfm.2025.10499 Published online by Cambridge University Press